Microphysical evolution in mixed-phase mid-latitude marine cold-air outbreaks

Seethala Chellappan,[1] Paquita Zuidema,[1] Simon Kirschler,[2] Christiane Voigt,[2] Brian Cairns,[3] Ewan C. Crosbie,[4] Richard Ferrare,[5] Johnathan Hair,[5] David Painemal,[4] Taylor Shingler,[5] Michael Shook,[5] Kenneth L. Thornhill,[5] Florian Tornow,[3] and Armin Sorooshian[6]

[1] *Department of Atmospheric Sciences, Rosenstiel School, University of Miami, Miami, Florida, USA*

[2] *Institut für Physik der Atmosphäre, Deutsches Zentrum für Luft- und Raumfahrt (DLR), Oberpfaffenhofen, Germany*

[3] *Goddard Institute for Space Studies, New York City, New York, USA*

[4] *AMA, Hampton, Virginia, USA*

[5] *NASA Langley Research Center, Hampton, Virginia, USA*

[6] *Department of Chemical and Environmental Engineering, University of Arizona, Tucson, Arizona, USA*

Seethala Chellappan's current affiliation: Analytical Mechanics Associates, Inc., Hampton, VA 23666, USA

Corresponding author: Paquita Zuidema, pzuidema@miami.edu and Seethala Chellappan, seethala.chellappan@ymail.com

Early Online Release: This preliminary version has been accepted for publication in *Journal of the Atmospheric Sciences*, may be fully cited, and has been assigned DOI 10.1175/JAS-D-23-0203.1. The final typeset copyedited article will replace the EOR at the above DOI when it is published.

ABSTRACT: Five cold-air outbreaks are investigated with aircraft offshore of continental northeast America. Flight paths aligned with the cloud-layer flow from January through March span cloud-top temperatures of -5 to -12 °C, *in situ* liquid water paths of up to 500 g m^{-2}, while *in situ* cloud droplet number concentrations exceeding 500 cm^{-3} maintain effective radii below 10 μm. Rimed ice is detected in the 4 colder cases within the first cloud pass. After further fetch, ice particle number concentrations reaching 2.5 L^{-1} support an interpretation that secondary ice production is occurring. Rime-splintering is clearly evident, with dendritic growth increasing ice water contents within deeper clouds with colder cloud-top temperatures. Buoyancy fluxes reach 400-600 W m^{-2} near the Gulf Stream's western edge, with 1-second updrafts reaching 5 m s^{-1} supporting closely-spaced convective cells. Near-surface rainfall rates of the 3 more intense cold-air outbreaks are a maximum near the Gulf Stream's eastern edge, just before the clouds transition to more open-celled structures. The milder 2 cold-air outbreaks transition to lower-albedo cumulus with little or no precipitation. The clouds thin through cloud-top entrainment.

Accepted for publication in *Journal of the Atmospheric Sciences.* DOI 10.1175/JAS-D-23-0203.1.

SIGNIFICANCE STATEMENT: Cold-air outbreaks off of the eastern US seaboard are visually spectacular in satellite imagery, with overcast, high-albedo clouds transitioning to more broken cloud fields. We use data from the recent NASA ACTIVATE (Aerosol Cloud meTeorology Interactions oVer the western ATlantic Experiment) aircraft campaign to examine the microphysics and environmental context of 5 such outbreaks. We find the clouds are not ice-deprived, but updrafts still supply significant liquid water. Cloud transitions are encouraged through near-surface rain for the deeper clouds, and otherwise clouds thin and break through mixing in drier air from above. These observations support understanding and further modeling examining how mixed-phase cloud microphysics affect cloud reflectivity and surface rainfall rates, important for both weather and climate forecasting.

1. Introduction

Cold-air outbreaks (CAOs) off of the eastern US seaboard provide dramatic visual examples of cloud morphology, with cloud streets and closed-cell circulations transitioning to more open-celled or thinner cloud structures with fetch. The CAOs typically occur behind cold fronts, suppressed by upper-level subsidence within the trough and trough-to-ridge portions of eastward-moving mid-latitude cyclones (Painemal et al. 2023). Coastal northerly winds turning eastward support strong moisture and heat fluxes off of the warm Gulf Stream (GS). The sea surface temperature (SST) gradient to the cold near-shore Labrador current further encourage secondary mesoscale circulations that aid cloud deepening (Liu et al. 2014; Naud et al. 2020),

Outflow of urban anthropogenic pollution elevate the cloud condensation nuclei (CCN) concentrations and cloud droplet number concentrations (N_d) (Corral et al. 2021; Dadashazar et al. 2021; Kirschler et al. 2022; Gryspeerdt et al. 2022). Space-based characterizations indicate super-cooled liquid, wherein produced ice can become melting snow (Field and Heymsfield 2015; Mülmenstadt et al. 2015; Matus and L'Ecuyer 2017). The precipitation in turn can alter the cloud morphology (Abel et al. 2017; Field et al. 2017). Mixed-phase CAOs represent a modeling challenge, in that the small-scale microphysical and turbulence processes must be accurately represented as well as the larger-scale synoptics. Interest in improving the understanding, modeling, and prediction of mixed-phase CAOs for both weather and climate has motivated multiple recent observational campaigns (Wendisch et al. 2019; McFarquhar et al. 2021; Geerts et al. 2022).

Accepted for publication in *Journal of the Atmospheric Sciences*. DOI 10.1175/JAS-D-23-0203.1.

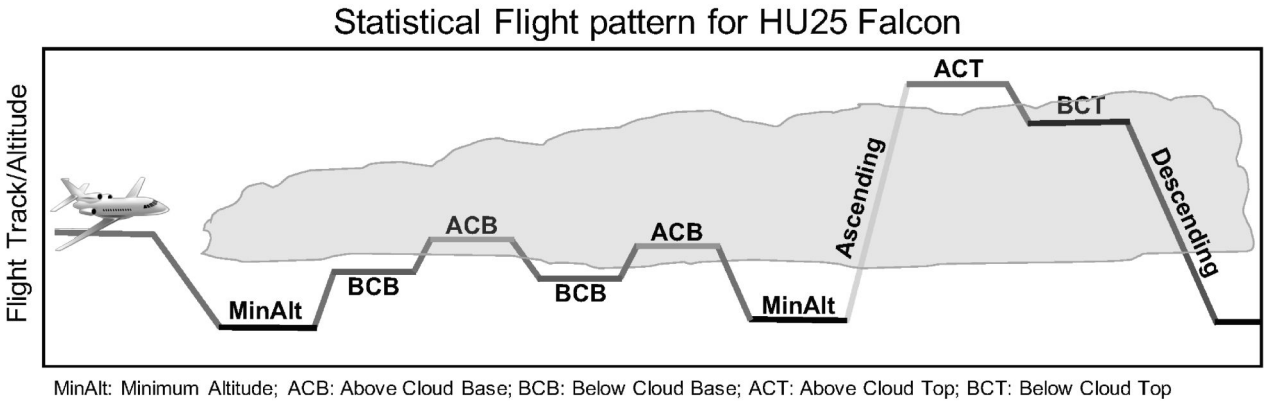

FIG. 1. Typical Falcon flight sampling plan. The same color coding and nomenclature is applied to each flight throughout the manuscript. The minimum altitude (MinAlt) legs occurred at ~ 150 m altitude. BCB=below cloud base, ACB=above cloud base, ACT=above cloud top, and BCT=below cloud top.

We contribute to this growing literature with detailed fetch-following characterizations of 5 winter days with CAOs over the northwest Atlantic (Table 1), using aircraft measurements from the NASA Earth Venture Suborbital-3 Aerosol Cloud meTeorology Interactions oVer the western ATlantic Experiment (ACTIVATE; Sorooshian et al. 2019), held from 2020 through 2022. A major observational strategy was to fly a high and low plane, both at speeds of ~ 120 m s^{-1}, within 5 minutes and 6 km of each other (Sorooshian et al. 2023). The low-flying Langley Falcon HU-25 plane followed a set flight pattern (Fig. 1) to collect *in-situ* cloud and aerosol microphysical measurements. At 8-9 km altitude, a King Air plane hosted the multiwavelength and depolarization-sensitive High-Spectral-Resolution Lidar-2 (HSRL-2) measuring aerosol and cloud profiles from which cloud top heights are retrieved, and a Research Scanning Polarimeter (RSP) measuring spectrally-resolved shortwave radiances from which cloud optical properties are retrieved. Dropsondes capture thermodynamic and wind profiles (approximately 4 per flight). The flight sampling encompasses approximately 1 day of the air mass advection. Although the plane speeds far exceed the air mass movement, the CAOs are quasi steady-state for a day, inferred from afternoon characterizations that resemble those from the morning flights.

The lower plane collected liquid cloud drop size distributions, and ice habit information from the Two-Dimensional Stereo (2DS) imager, but did not sample ice-nucleating particles (INP). We primarily infer evidence for secondary ice production (SIP) through comparison to the Welti et al. (2020) INP parameterization based on a best-fit to multiple measurement datasets: INP=(T+5)*(-

Accepted for publication in *Journal of the Atmospheric Sciences.* DOI 10.1175/JAS-D-23-0203.1.

10^{-5}*exp(500/T+60)) with T in Celsius and INP in m^{-3}. This equation estimates an INP concentration of 0.0011 L^{-1} at -10 °C, reducing to zero at -5 °C. This parameterization incorporates data from Irish et al. (2019) on marine boundary layer immersion INP concentrations off the eastern Nova Scotian coast during the summer of 2014. Electron microscopy identified the INP aerosol as mineral dust. Soil aerosols are likely contained in the continental outflow affecting ACTIVATE CAOs, though we were not able to identify the dust as such. Sea spray aerosol, generated through wave breaking and bubble bursting, produce fewer INP, by 2-3 orders of magnitude, at -15 °C, compared to land sources globally (DeMott et al. 2016; McCluskey et al. 2018), with contributions from marine biogenic activity less well known for this region (Creamean et al. 2022; Haëck et al. 2023).

Section 2 outlines the datasets used for this study, Section 3 provides the environmental context, and Section 4 details the flights occurring on the 5 days. A description of the *in situ* microphysical, temperature and vertical velocity characteristics is integrated with remotely-retrieved cloud top heights, sea surface temperatures (SST) and reanalysis-derived surface fluxes. After describing each flight, we examine how ice microphysical quantities and near-surface precipitation depend on cloud-top temperature (T_{ct}), *in situ* temperature and satellite-retrieved liquid water paths (LWPs). Section 5 further discusses ice production processes and boundary layer thermodynamic coupling, towards developing a holistic view of mixed-phase cloud evolution in mid-latitude cold-air outbreaks. We document the sub-cloud rainfall rates and place them into context with any cloud morphological transitions. An online Supplement provides supporting documentation, and the Appendix contains a comparison of remotely-retrieved to *in-situ* liquid cloud properties. The 5 days drawn from March 2020 and January-March of 2021 (Table 1) provide a range of cloud conditions. The data from the 8 research flights do not support a comprehensive analysis, but do support a framework in which further data analysis can be inserted, and extend beyond case-specific findings.

2. Datasets

Research flights lasted near 4 hours with both morning and afternoon flights occurring on select days (Table 1). The instrument datasets and their characteristics are summarized in Table 2, with further select details provided below.

Accepted for publication in *Journal of the Atmospheric Sciences*. DOI 10.1175/JAS-D-23-0203.1.

TABLE 1. Dates, research flight numbers, plane participation and dropsonde number for each flight day.

date	morning	am dropsondes	afternoon	pm dropsondes
1 March 2020	RF13, both planes	circle of 11	RF14, both planes. no RSP*	2
29 January 2021	RF42, King Air (high flying)	2	RF43, Falcon (*in-situ*)	0
3 February 2021	RF44, both planes	5	–	–
5 March 2021	RF49, both planes	5	RF50, both planes	2
8 March 2021	–	–	RF51, both planes	4

*Research Scanning Polarimeter

a. In situ Microphysics

A Fast Cloud Droplet Probe (FCDP) and a 2DS imager, operated by the Deutsches Zentrum für Luft- und Raumfahrt (DLR), and a Cloud Droplet Probe (CDP) operated by NASA Langley, collected the *in situ* cloud water information. A cloud droplet number concentration (N_d), liquid water content (LWC) and effective radis (r_e) can be derived from each probe's measurements. High aerosol loadings challenge the FCDP and CDP N_d measurements, detailed in the Appendix. Lacking a clear justification to prefer one instrument over the other, we average the FCDP and CDP N_d unless otherwise stated. On the 3 February 2021 flight, the FCDP probe iced, and only corrected (described in the Appendix) CDP data are shown.

The diameters measured by the FCDP and 2DS probes overlap between 11.4 to 50 μm. A combined size distribution is constructed from diameters spanning 3 to 1465 μm, from which the liquid cloud properties are identified for three separate diameter ranges: cloud (< 40 μm), drizzle (40-108 μm) and rain (> 108 μm). The 40 μm diameter threshold corresponds to when collision-coalescence first becomes active (Jonas 1996), while ~100 μm diameter drops can reach the surface for conventional humidities and cloud base heights (Pruppacher and Klett 1997). Precipitation rates are only calculated for liquid drops, based on the measured size distribution of spherical-only particles and the Wood (2005) fall velocity parameterization.

The 108 μm diameter threshold also corresponds to when ice can be discriminated from liquid by the 2DS cloud probe using particle asphericity (Kirschler et al. 2023). Corrections are applied for image distortion, sample area and shattering. The ice water content (IWC) is calculated using the Baker and Lawson (2006) area-to-mass parameterization and ice particle number concentration (N_i) following Korolev et al. (1998), for non-sherical particles > 100 μm. The 2DS detection limit for ice particle concentrations is 10^{-4} cm^{-3} at 1 Hz, with the analysis limited to non-zero N_i.

Accepted for publication in *Journal of the Atmospheric Sciences*. DOI 10.1175/JAS-D-23-0203.1.

TABLE 2. Instrument datasets*

Instrument	Measurement	Resolution	Uncertainty	Reference
SPEC Inc. Fast Cloud Droplet Probe (FCDP)	r_e, N_d, LWC	3-50 μm	up to 50%/ 10%/40%	Kirschler et al. (2022)
DMT Cloud Droplet Probe (CDP)	r_e, N_d	3-50 μm	20%	Lance (2012)
SPEC Inc. Two-Dimensional Stereo (2DS)	IWC,N_i, habit	11.4-1465 μm	up to 60%10%	Kirschler et al. (2023)
Turbulent Air Motion Measurement System (TAMMS)	w	20 Hz	10 cm s^{-1}	Thornhill et al. (2003)
Rosemont 102 sensor	T	0.05 s	0.5 °C	–
NRD41 Dropsondes	p, T, q, wind	~ 11 m	0.5 hPa/0.2°C/3%/0.5 m s^{-1}	Vömel et al. (2023)
High Spectral Resolution Lidar-2 (HSRL-2)	cloud top height	~ 5 m	~ 5 m	Sorooshian et al. (2023)
HSRL-2	ice/water phase	–	~ 10%	Hu et al. (2009)
Research Scanning Polarimeter (RSP)	r_e (cloud-top)	100m x 600m	~ 1 μm	Alexandrov et al. (2012)
RSP	τ	100m x 600m	10%	Nakajima and King (1990)

* symbols explained in text

Optical interactions with small ice columns can generate Poisson focus points with the appearance of an 'H' (Vaillant de Guélis et al. 2019).

Individual flight legs last 2 to 4 minutes, with most of the analysis relying on leg-means constructed from 1 Hz data. Leg-mean N_d are constructed from 1 Hz LWCs exceeding 0.01 g m^{-3} and $N_d > 10$ cm^{-3}, similar to Kirschler et al. (2023), during Below Cloud Top (BCT), Above Cloud Base (ACB), Below Cloud Base (BCB), and Minimum Altitude (MinAlt, at ~150 m altitude) level legs (Fig. 1). Leg-mean rainrates are calculated from 1 Hz rainrates > 0.01 mm hr^{-1}. During the 4-minute profile legs the plane travels a horizontal distance of ~ 24 km. This means horizontal cloud heterogeneities can become aliased into the profiles.

b. Remotely-Sensed Variables, Reanalysis, and Other

The HSRL-2 identifies the cloud top height through attenuation, and the ratio of the volume extinction coefficient to the backscattered intensity (the lidar ratio) helps indicate the ice and water phase (Hu et al. 2009). Ice can increase the lidar ratio because the refractive index for ice is slightly above that expected for water spheres of the same size. The RSP retrieves cloud optical depth (τ) and cloud-top effective radius (r_e) (Table 2), from which a liquid water path (LWP) can be estimated assuming an adiabatically-distributed LWC profile. MODIS-derived τ and r_e are more prone to retrieval artifacts (see Appendix), but MODIS LWPs are more readily available than those from RSP and cover a larger spatial domain. We rely on MODIS LWP to support a comparison across the flights. Cloud top temperature (T_{ct}) is determined from ERA5 temperatures colocated with

Accepted for publication in *Journal of the Atmospheric Sciences*. DOI 10.1175/JAS-D-23-0203.1.

HSRL-2 cloud-top altitudes. The ERA5 T_{ct} correspond more closely to dropsonde-determined values than do the MODIS estimates (Fig. S1), which can be influenced by surface temperatures (Zuidema et al. 2009). The ERA5 T_{ct} is nevertheless still warmer than some of the BCT leg-mean *in situ* temperatures, indicating ERA5 T_{ct} can also have a warm bias. Global High-Resolution (1 km) satellite Sea Surface Temperature (GHRSST) contours of 294 K are chosen to indicate the Gulf Stream (GS) boundaries, as ERA5's grid spacing of 31 km unrealistically broadens the Gulf Stream (Seethala et al. 2021).

ERA5 reanalysis establishes the intensity of a cold-air outbreak using $M = \theta_{SKT}$ - θ_{850hPa} where θ_{SKT} is the 'skin' SST potential temperature, following Papritz et al. (2015). ERA5 buoyancy fluxes (Q_B) are calculated from the latent (Q_L) and sensible (Q_S) fluxes as $Q_B = Q_S * (1 + 0.6q_{2m}) + 0.6Q_L \frac{c_p}{L_v} T_{2m}$, where q_{2m} and T_{2m} are the specific humidity and temperature at 2 meters, c_p is the specific heat of air at constant pressure and L_v is the latent heat of vaporization. Lagrangian forward trajectories, based on ERA5 data at 500 m altitude combined with the HYSPLIT air trajectory model, initialized upstream of the flight path, assess how well the flight tracks follow the boundary layer flow. No radar was deployed on either plane, nor a Nevzorov total water content cloud probe (useful for constraining bin-resolved ice+liquid water contents).

3. Overview

Three days contained both morning and afternoon flights (March 1 2020, 29 January 2021 and 5 March 2021) (Table 1). All but the morning flight on 1 March, 2020 followed a flight track approximately aligned with the Lagrangian boundary layer trajectories (Fig. 2, top row). All flights cross the western GS edge, with SST increases typically exceeding 10 °C along the flight tracks (Fig. 2, 2nd row; Fig. 3b), and maximum SSTs reach 24 °C, decreasing slightly further eastward. Near-surface ERA5 wind speeds range from 4 to 20 m s $^{-1}$, mostly increasing eastward (Fig. 2, 2nd row; Fig. 3a), in accord with a surface wind convergence over the warmer waters (Minobe et al. 2008; Small et al. 2008; Plagge et al. 2016). Buoyancy fluxes and the Bowen ratio are nevertheless a maximum at the western GS edge, decreasing further east as air-sea temperature differences reduce (not shown). The 750 hPa vertical velocities indicate synoptic subsidence (Fig. 2, third row), except on 3 February, 2021. We show later that 750 hPa is still within the boundary layer on

Accepted for publication in *Journal of the Atmospheric Sciences.* DOI 10.1175/JAS-D-23-0203.1.

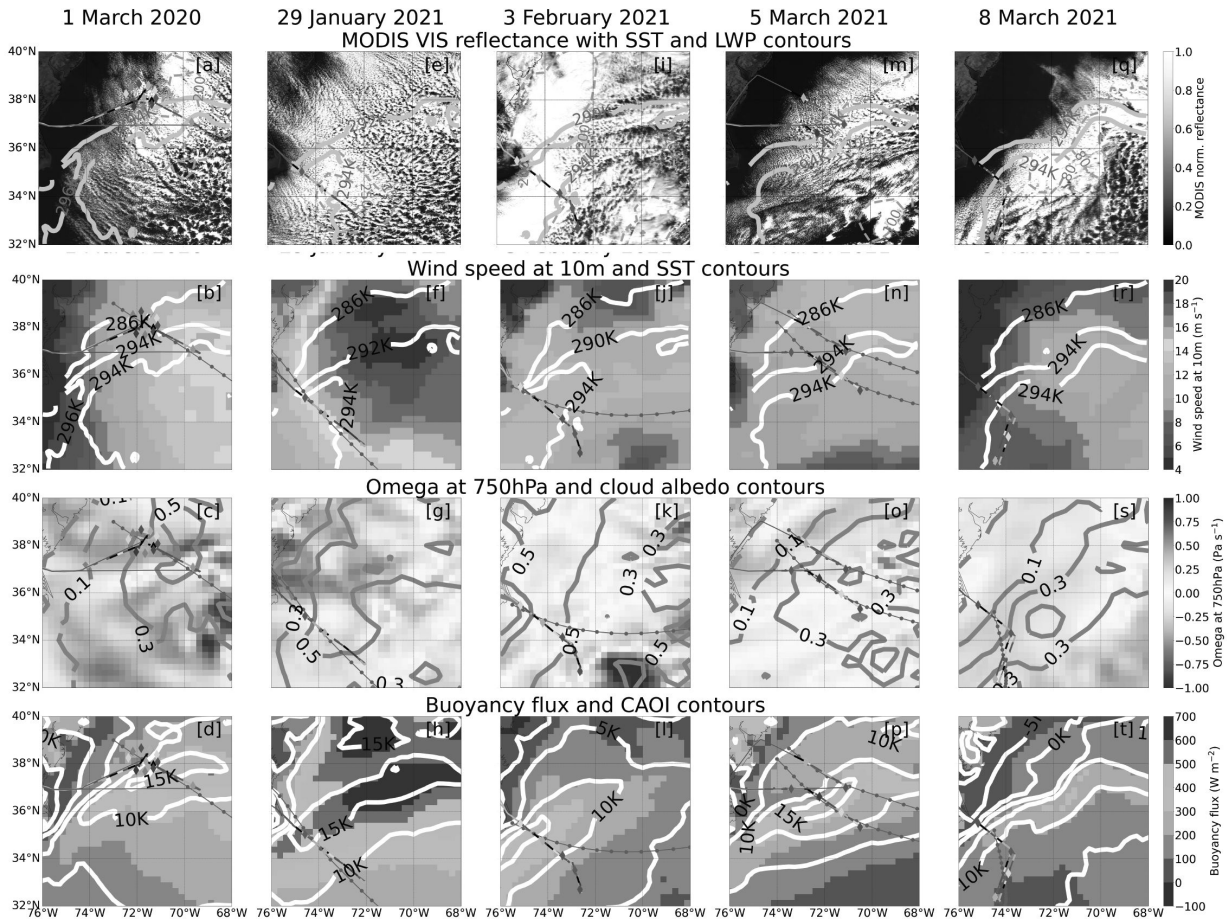

FIG. 2. Top row: MODIS visible imagery, with SST contours at 290K, 292K and/or 294K (dusty blue line), MODIS LWPs at 80, 100, 150, 200 and/or 250 g m^{-2} (dashed orange lines), and the Falcon flight tracks, color-coded by altitude and with dropsonde locations indicated (purple diamonds) for a) 1 March 2020, b) 29 January 2021, c) 3 February 2021, d) 5 March 2021 and e) 8 March 2021. 3 February image is from *Terra*, the others from *Aqua*. Second row: ERA5 10m wind speed with SST contours overlaid, Third row: ERA5 vertical velocities at 750 hPa (color) with CERES-MODIS cloud albedo in grey contours; and bottom row: ERA5 buoyancy fluxes (color) overlaid with CAO *M* index (white contours). HYSPLIT trajectories (dark green) initialized at a)-d): 15 UTC 1 March 2020 at 39°N, 73°W, e)-h): 15 UTC 29 January 2021 at 36.8°N, 75.5°W, j)-l): 14 UTC 3 February 2021 at 35.5°N, 75.5°W, m)-p): 11 UTC 5 March 2021 at 38.2°N, 74°W (am) and 15 UTC at 38.65°N, 73.5°W (pm), and q)-t): 8 March 2021 trajectory initialized at 15 UTC, 35.2°N, 74.5°W.

this day. Surface buoyancy fluxes align well with the Gulf Stream boundaries (Fig. 2, bottom row) as does the CAO *M* index.

Accepted for publication in *Journal of the Atmospheric Sciences.* DOI 10.1175/JAS-D-23-0203.1.

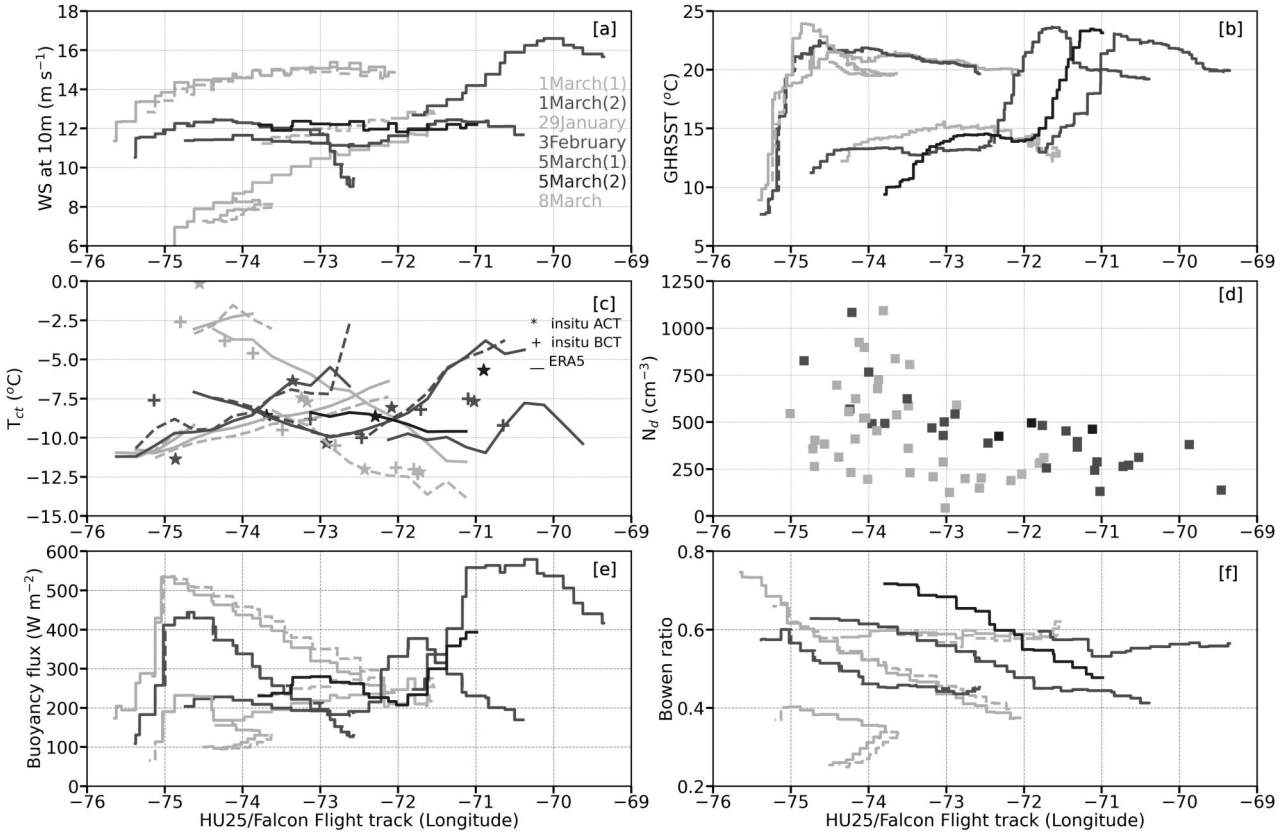

FIG. 3. Meteorology and N_d along the Falcon flight tracks as a function of longitude: a) 10m ERA5 wind speed, b) SST, c) *in situ* and ERA5 T_{ct}, d) Leg-mean N_d (ACB and BCT), e) ERA5 buoyancy fluxes and f) ERA5 Bowen ratio, for outbound and inbound (return) flight tracks (solid and dashed lines, respectively). Morning/afternoon flights on 1 and 5 March indicated by (1) or (2) respectively.

Maximum MODIS liquid water paths range from 80 g m^{-2} to 250 g m^{-2} (Fig. 2, 1st row). *In-situ* leg-mean N_d decrease with distance offshore from over 800 cm^{-3} to ~ 200 cm^{-3} (Fig. 3d). T_{ct}s are a minimum of ~ -11 °C to the west, increasing consistently with fetch to ~ -5 °C further east (Fig. 3c; the 1 March morning flight is anomalous because its track parallels the GS). Corresponding values along the Lagrangian trajectories correspond well to those perceived during the flights (Fig. S2). This supports the steady-state assumption that the *in situ* information along the flight track can serve as a proxy for the Lagrangian evolution. Dropsonde profiles of temperature (T), potential temperature (θ) and relative humidity (RH) indicate boundary layer deepening and near-surface warming as the air masses advect to the east, and suggest boundary layers often remain well-mixed (Fig. S3).

Accepted for publication in *Journal of the Atmospheric Sciences.* DOI 10.1175/JAS-D-23-0203.1.

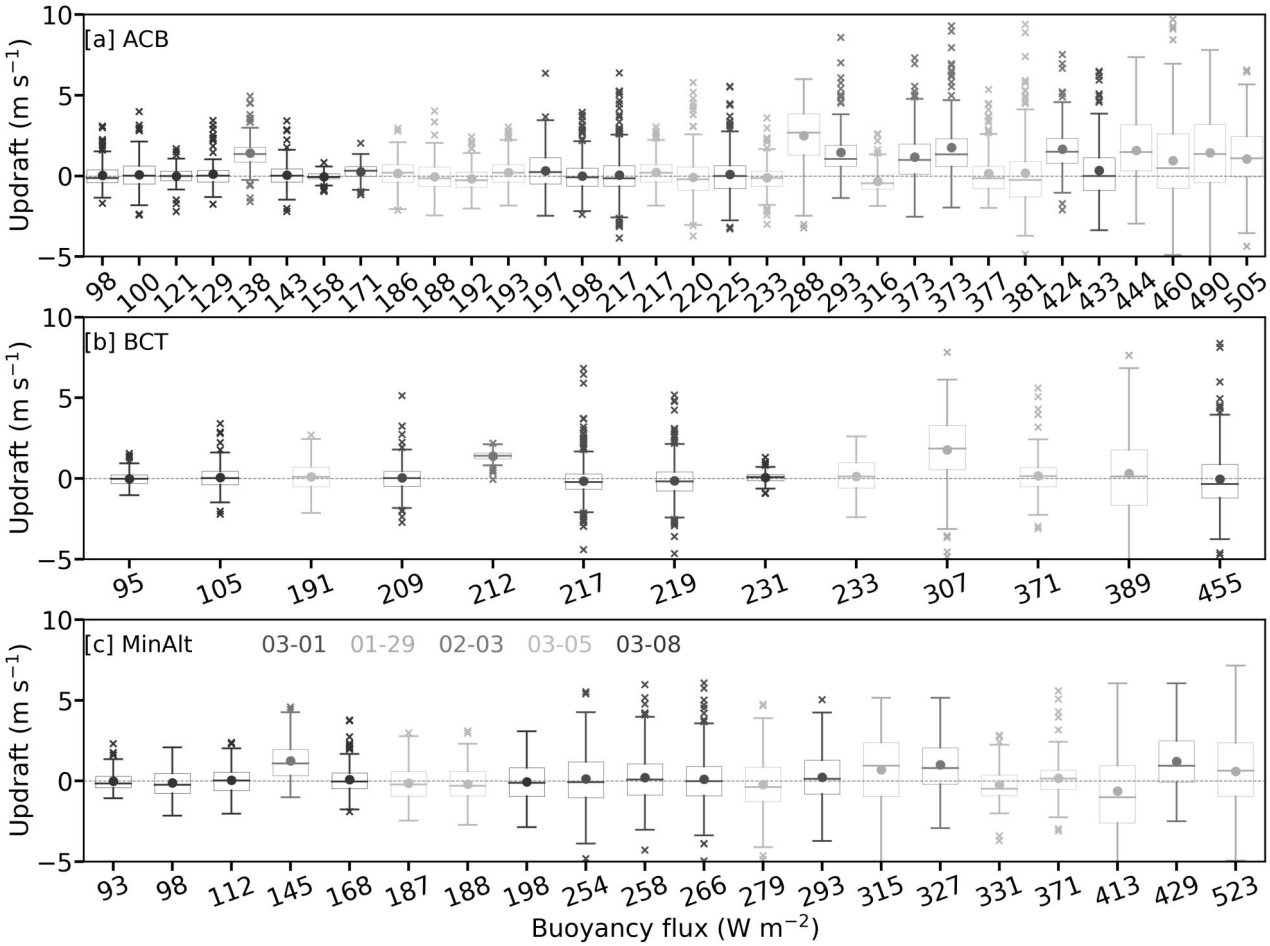

FIG. 4. Histograms of 1 Hz vertical velocities as a function of the buoyancy fluxes for a) above-cloud-base, b) below-cloud-top, and c) minimum altitude level legs. Colors indicate flight date, means by filled circles, medians, ± 25% percentiles by lines.

Updrafts are strongest at the western GS edge, in concert with the surface buoyancy fluxes (Fig. 4). The upper quartile of the 1 Hz updrafts often exceed 2 m s^{-1} (see also Fig. S4), with maximum individual 1 Hz values reaching 10 m s^{-1}. Updrafts are generally stronger near cloud base than below cloud top (Fig. 4). 1 Hz downdrafts reach minima of -5 m s $^{-1}$, with the lowest quartile occasionally stronger than -2 m s^{-1}. The earliest CAO within the year, on January 29 2021, experienced the strongest surface wind speeds, surface fluxes, updrafts and M values of the 5 days, followed by 3 February 2021. The latest CAO, on 8 March 2021 was the weakest CAO of the 5 days, inferred from M and the wind speeds (Figs. 2-3).

Accepted for publication in *Journal of the Atmospheric Sciences.* DOI 10.1175/JAS-D-23-0203.1.

4. Microphysical characterization of the five days

A satellite image is superimposed with the flight track using the color-coding conventions of Fig. 1, followed by height-time series of flight tracks their *in situ* temperatures and selected time-stamped 2DS imagery in Figs. 5, 7, 9, 12 and 15. Profiles of microphysical quantities are shown for 1 March 2020, 29 January 2021 and 3 February 2021 in Figs. 6, 8, 10, and 14, from 5 and 8 March 2021 in Figs. S5 and S7 and the flight track for 8 March 2021 in Fig. S6.

a. 1 March 2020

1) MORNING

The morning flight paralleled the western GS edge, sampling perpendicular to the dominant boundary layer flow. The flight nevertheless first sampled clear air, then thin cloud deepening into an overcast region with MODIS-derived LWPs of 100-200 g m^{-2}, wherein a circle of 11 dropsondes was released (Fig. 5). Rimed ice is already noticeable within the first cloud pass, a thin cloud of primarily small super-cooled droplets (Fig. 5c, left-hand image) at an *in situ* temperature of -8 °C (Fig. 5b) and leg-mean N_d exceeding 800 cm^{-3}.

Accepted for publication in *Journal of the Atmospheric Sciences.* DOI 10.1175/JAS-D-23-0203.1.

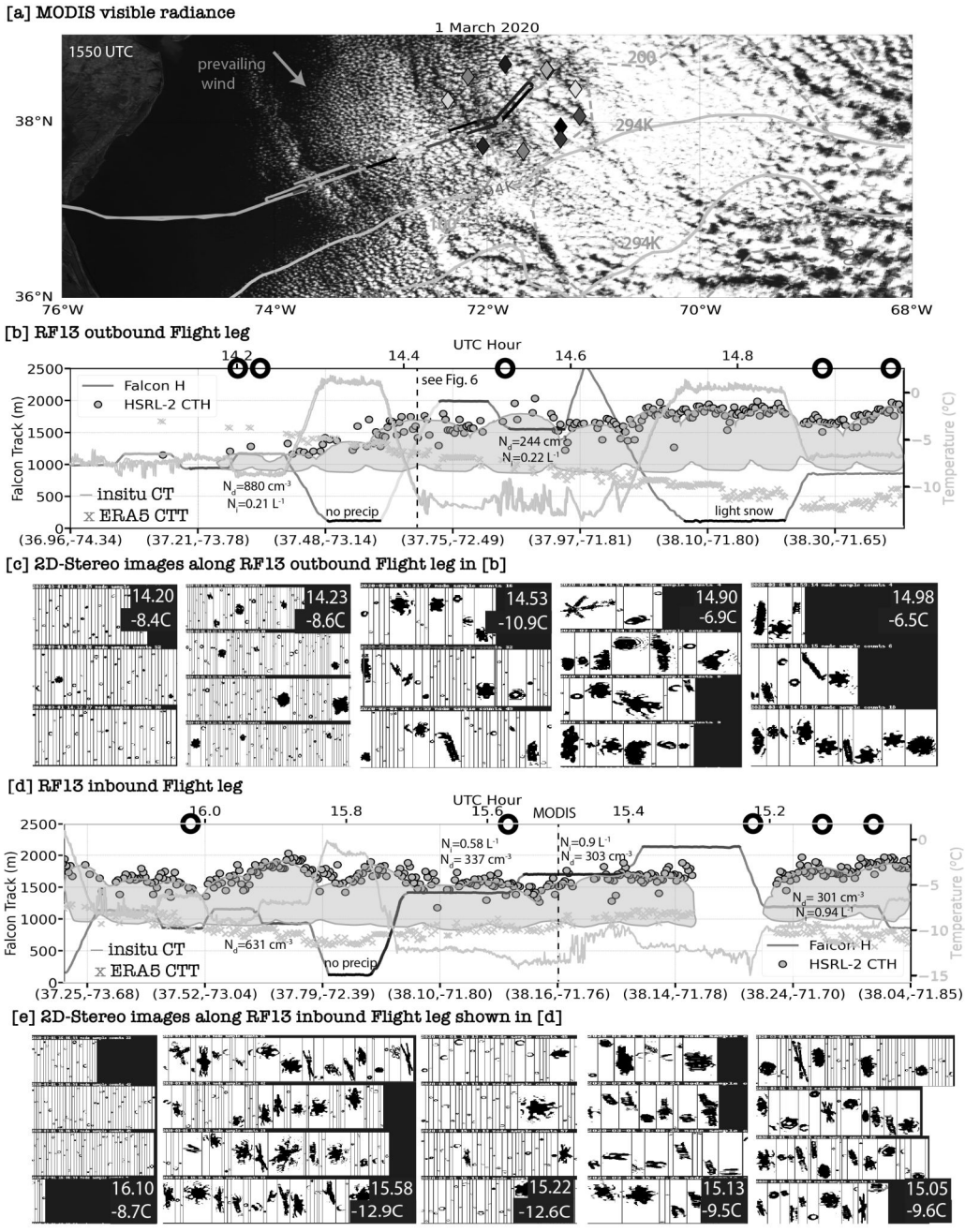

FIG. 5. 1 March 2020 morning flight (RF13). a) MODIS visible imagery with flight track superimposed, color-coded according to Fig. 1 and dropsondes (diamonds). SST contour of 294K in blue lines, MODIS LWPs of 100 and 200 g m^{-2} in dashed orange lines. b) HSRL2-inferred cloud top height (circles), altitude flight path (color-coded), *in situ* temperatures and ERA5 T_{ct} (light blue line and crosses; right-hand y-axis) for the outbound flight. Circles along upper x-axis correspond to 2DS imagery times in c). d)-e): same as b)-c) for the return inbound leg; time along upper x-axis increases from right to left. b), d): N_d, N_i indicated for ACB (orange) and BCT (blue) legs. Cloud depiction is a schematic.

Accepted for publication in *Journal of the Atmospheric Sciences.* DOI 10.1175/JAS-D-23-0203.1.

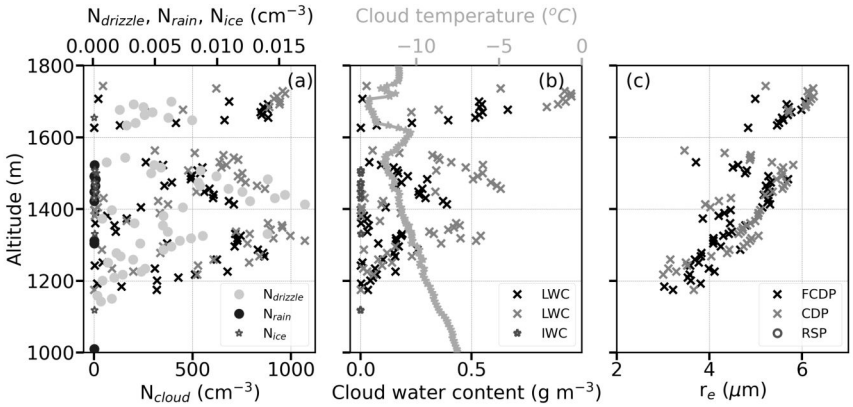

FIG. 6. *In-situ* ascent of 1 March 2020 morning (RF13) at 14.4 UTC, 37.65 °N, 72.72 °E of a) cloud (CDP and FCDP, grey and black asterisks) and drizzle (r> 20μm), rain (r > 58 μm) and ice number concentrations (yellow, blue and red circles respectively, FCDP+2DS combined distribution), b) cloud water contents (CDP and FCDP, grey and black asterisks, LWP= 84 and 161 g m^{-2} respectively) and temperature (grey), and c) FCDP and CDP droplet effective radius (r_e, black and grey asterisks respectively).

Accepted for publication in *Journal of the Atmospheric Sciences.* DOI 10.1175/JAS-D-23-0203.1.

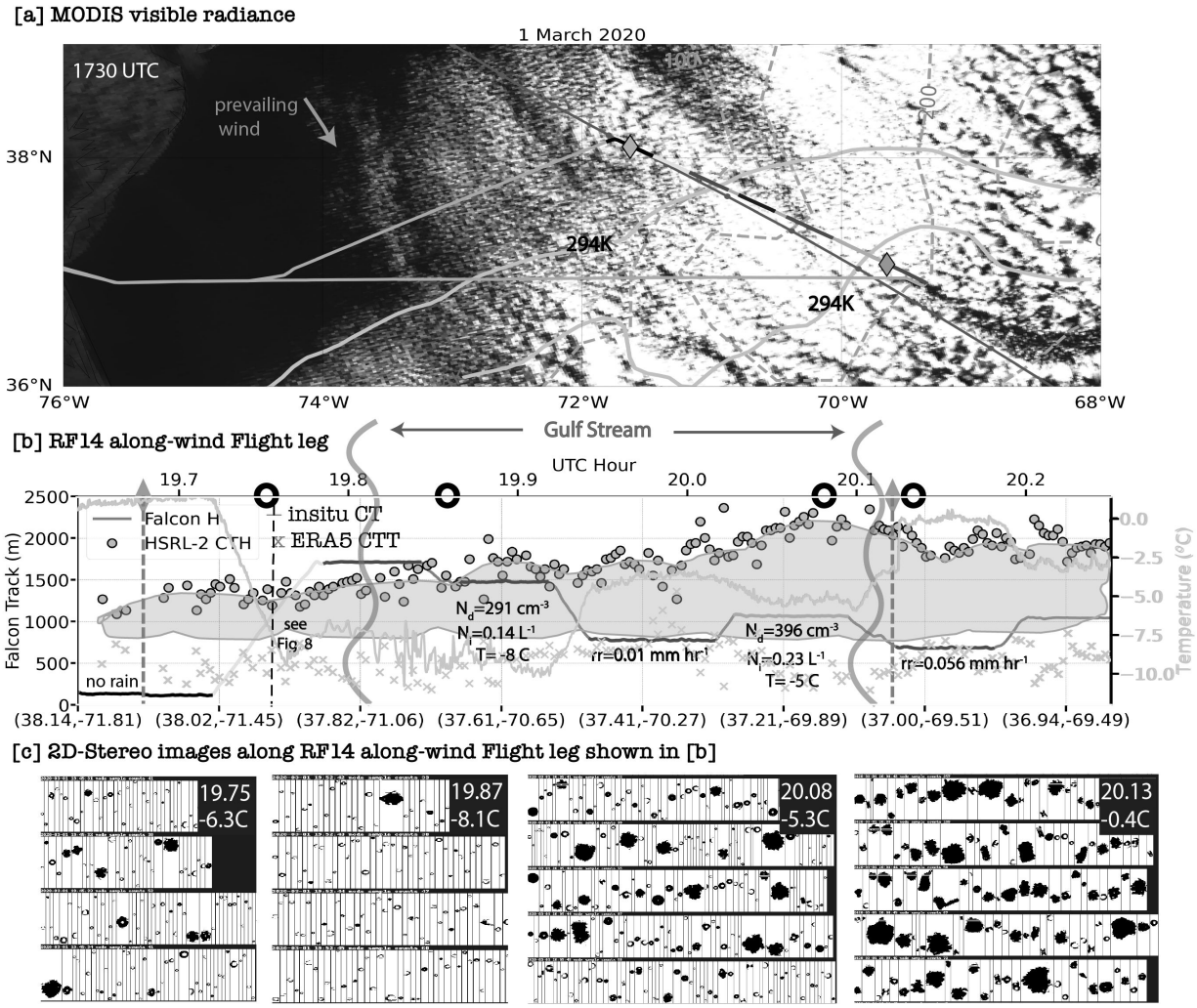

FIG. 7. 1 March 2020 afternoon flight (RF14). Similar notation to Fig. 5. No RSP data. 19.75 UTC ascent profiled in Fig. 8. Curved pink lines indicate location of the Gulf Stream (294K SST contour) throughout.

Within the more developed, stratiform cloud region, dendrites and large rimed ice particles occur under a T_{ct} of ~ -12 - -13° °C. Cloud top heights reach ~ 1.8 km. N_i reaches almost 1 L^{-1} at the northeast end of the flight, where the leg-mean N_d decreases to < 300 cm^{-3}.

Only light precipitation (snow and a few rimed ice particles) occur on the easternmost MinAlt leg at 14.8 UTC, at temperatures barely above 0 °C. Dropsondes show mostly well-mixed boundary layers (Fig. S3). The first profile, an ascent through cloud with a LWP of ~ 100 g m^{-2} (Fig. 6), shows an inversion-capped cloud layer reaching ~ 1.5 km, with another cloud layer capped at 1.8 km. Surface buoyancy fluxes reach 200 W m^{-2} (Fig. 3e), supporting vertical velocities of 2-4 m s^{-1} (Figs. 4 and S4). The dropsondes capture a range of inversion heights, often capped

Accepted for publication in *Journal of the Atmospheric Sciences.* DOI 10.1175/JAS-D-23-0203.1.

by multiple stable layers, consistent with a range of cloud top heights and/or detrainment layers. Cloud-top r_e remain below 6 μm, consistent with $N_d > 700$ cm^{-3}. N_i and IWCs are highest at cloud temperatures between -9.5 °C and -12.5 °C, colocated with the LWC maximum, with some drop radii > 20 μm during an ascent through cloud with LWP of ~ 100 g m^{-2} (Fig. 6).

2) AFTERNOON

In contrast to the morning, the afternoon research flight is well-aligned with the boundary layer flow, crossing over the GS from 19.8 UTC to 20.1 UTC and briefly sampling more open-celled convection at 20.2 UTC (Fig. 7). Just west of the GS, an ascending profile samples rimed ice within a layer of predominantly super-cooled water droplets at temperatures ~ -6 °C (Fig. 7c, first image). N_d decreases with altitude and is less than in the morning (Fig. 8; 250-400 cm^{-3} versus 500-800 cm^{-3}). Over the GS, MODIS LWPs and cloud top heights reach 200 g m^{-2} and 2.3 km respectively, above a slightly stable boundary layer ($\frac{\partial \theta}{\partial z} \sim 2$ K km^{-1}, from dropsonde data shown in Fig. S3). The cloud base warms as the flight progresses, with the first BCB leg at 20 UTC occurring at ~ -3 °C and the second at 20.15 UTC near 0 °C, despite similar altitudes of ~ 700 m. Light rain is mixed with some aggregates during the first BCB leg (not shown). At higher altitudes rimed ice particles co-exist with supercooled droplets at -5 °C (2DS image at 20.08 UTC in Fig. 7c, and Fig. 8). The leg-mean rainrate increases to 0.056 mm hr^{-1} during the second BCB leg, mixed in with large snow aggregates and a few columns (Fig. 7c, at 20.13 UTC), just prior to the transition region to a more open-celled cloud structure. N_i also increases towards the east as the clouds deepen (Fig. 7b).

b. 29 January 2021

This CAO is the earliest within the seasonal cycle, with the 294 K SST contour barely reaching the ACTIVATE domain from the south (Fig. 2e). Morning and afternoon flights sample mostly visually-overcast regions with MODIS LWPs > 250 g m^{-2} and are just able to reach the open-celled cloud structure east of the GS. ERA5 10-m winds exceed 14 m s^{-1} in places (Fig. 3a), supporting buoyancy fluxes > 500 W m^{-2} at the western GS edge (Fig. 2h) and 1 Hz ws > 5 m s^{-1} (Figs. 4, S4). The two morning dropsondes, released near the eastern and western GS edges respectively,

Accepted for publication in *Journal of the Atmospheric Sciences*. DOI 10.1175/JAS-D-23-0203.1.

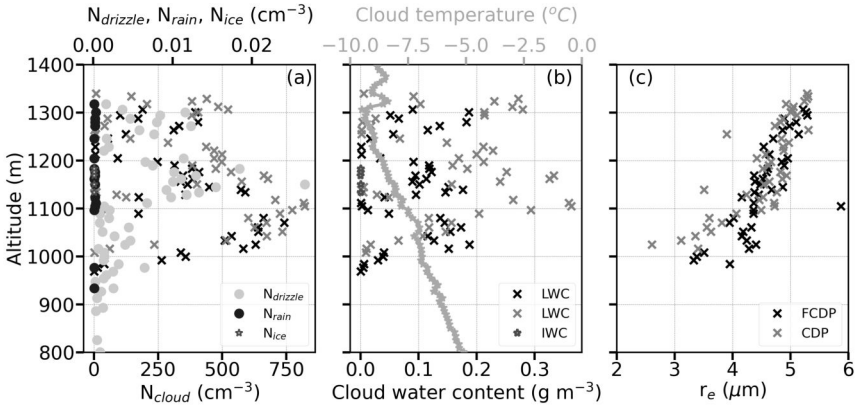

FIG. 8. 1 March 2020 afternoon (RF14) *in-situ* ascent at 37.95°N, 71.31°E, 19.75 UTC of a) cloud, drizzle, rain and ice number concentrations, FCDP+2DS, b) cloud water content and temperature (CDP and FCDP, grey and black asterisks, LWP= 30 and 51 g m^{-2} respectively), and c) r_e.

separated by a distance of ~ 100 km, indicate a deepening of a relatively well-mixed boundary layer from ~ 1.7 km to ~ 2 km (Fig. S3).

Accepted for publication in *Journal of the Atmospheric Sciences.* DOI 10.1175/JAS-D-23-0203.1.

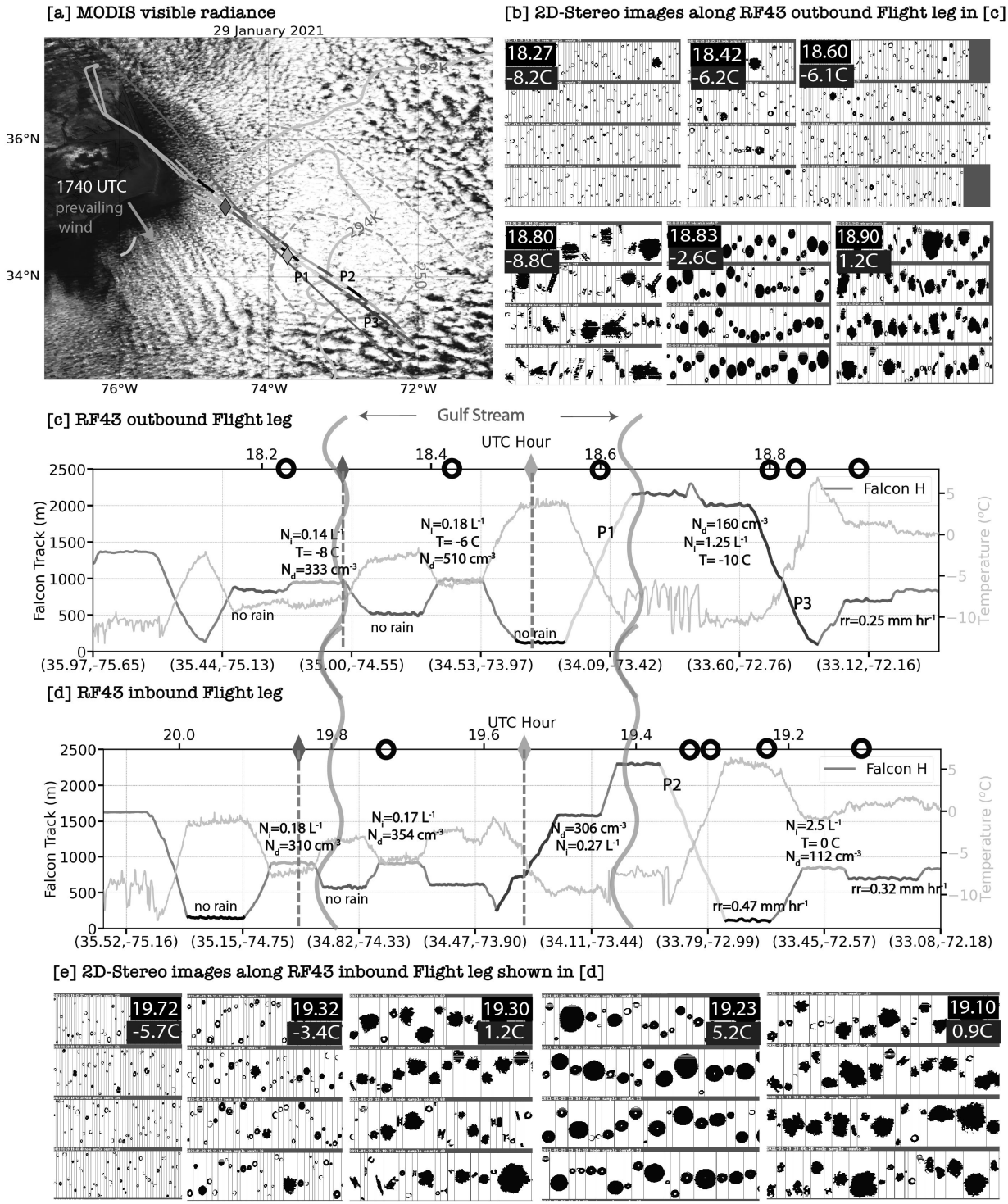

FIG. 9. 29 January 2021 afternoon (RF43). Similar notation to Fig. 5. Morning dropsonde locations shown. See Fig. 10 for *in situ* profiles P1, P2 and P3.

Accepted for publication in *Journal of the Atmospheric Sciences.* DOI 10.1175/JAS-D-23-0203.1.

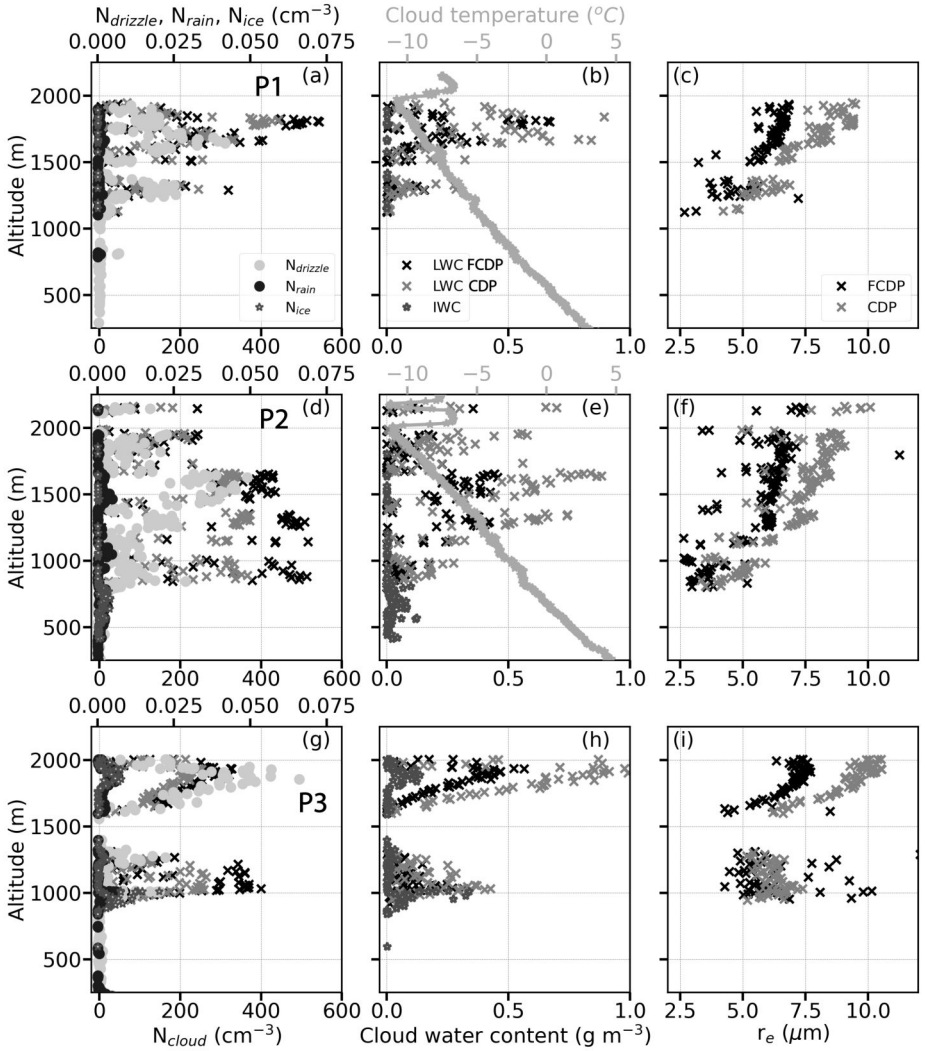

FIG. 10. 29 January 2021 afternoon (RF43) *in-situ* profiles organized from west (top) to east (bottom). a)-c): P1, ascent at 18.6 UTC, 34.13°N, 73.46°W (FCDP, CDP LWP=93, 225 g m^{-2} resp.) over the eastern GS flank. d)-f): P2, 19.35 UTC ascent at 33.83°N, 73.04°W (FCDP, CDP LWP=121, 260 g m^{-2} resp.), just east of the GS. g)-i): P3, descent at 18.8 UTC, 33.43°N, 72.55°W (FCDP, CDP LWP=154, 305 g m^{-2} resp.), further east of the GS. P3's temperature reading was affected by icing and is not shown. Conventions as in Fig. 6.

The first ACB leg just west of the GS measured a leg-mean N_d of 330 cm^{-3} at a temperature of -8.2 °C (Fig. 9). A rimed/aggregated ice particle is already present within the cloud of small droplets (first image in Fig. 9b). Deeper clouds further east reach an *in-situ* T_{ct} near -10 °C at 18.75 UTC, with the thickest cloud at and east of the eastern GS edge. Rimed and aggregated snow particles are present along with a few columns (e.g. the 2DS imagery at 18.8 UTC). By 18.9 UTC, during the easternmost flight portion, the BCB leg temperature has risen to 2 °C, and leg-mean rain

Accepted for publication in *Journal of the Atmospheric Sciences*. DOI 10.1175/JAS-D-23-0203.1.

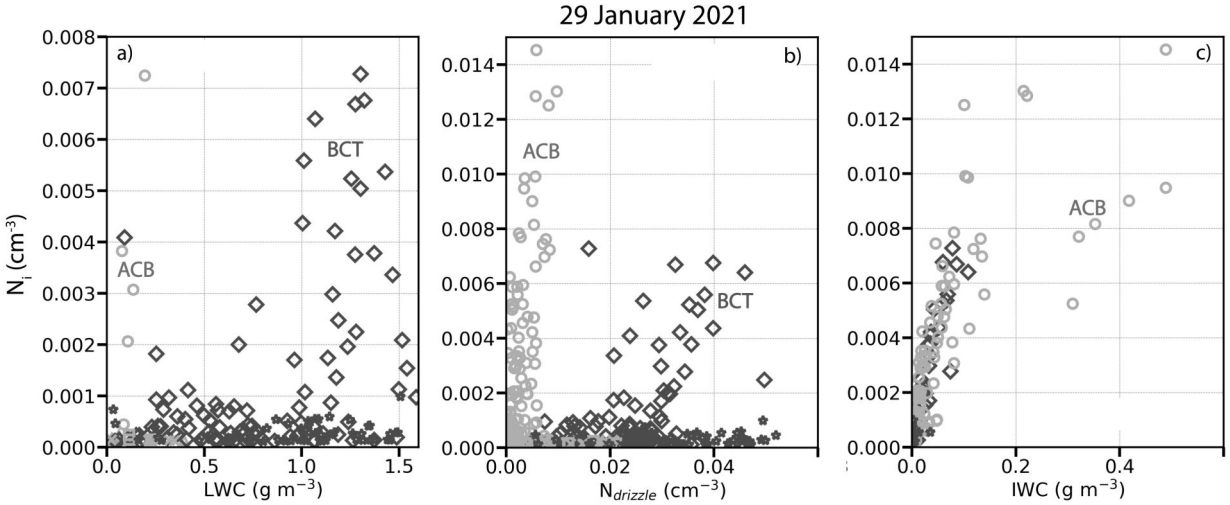

FIG. 11. N_i vs a) LWC, b) $N_{drizzle}$, and c) IWC for the ACB (pink) and BCB (green) legs from 29 January 2021 (RF43), using 1Hz data. Note y-axis range for N_i differs between a) and b),c).

rates reach 0.25 mm hr^{-1}, increasing to 0.47 mm hr^{-1} for the lower MinAlt leg. Snow aggregates below cloud base become rain by 150 m above the ocean surface, preceeding the transition to a more open-celled cloud morphology.

Three *in situ* profiles occur within 45 minutes and 110 km of each other, either directly over or slightly east of the Gulf Stream (Fig. 10). These are shown arranged from west to east (top to bottom) in Fig. 10, with profile P3 preceeding profile P2 in time. For all three profiles, the T_{ct} and cloud top height remain at -10 to -11 °C and 2 km respectively. Probe-mean (the average of FCDP and CDP values) profile LWPs increase from 160 to 230 g m^{-2} with fetch. Rainfall also increases eastward. *In-situ* BCT r_e remain ≤ 9 μm, however, with maximum N_d ranging between 400-500 cm^{-3}.

Although all 3 profiles appear to sample two (or more) distinct cloud layers, this may reflect slant-paths through clouds with different bases and tops. Profile P1, an ascent at 18.6 UTC over the eastern GS, samples a thermodynamically well-mixed boundary layer (Fig. 10a-c). The 0 °C level is at ~ 500 m, below a cloud base at 1.2 km of -5°C, and the cloud top is strongly capped by a 5K temperature inversion (Fig. 10b). N_d increases to 550 cm^{-3} near the upper cloud top, within the highest LWCs of the profile. The increase in N_d with height suggests the N_d reduction near cloud base occurs primarily through collision-coalescence. Despite BCT r_e of only ~ 8 μm, some

Accepted for publication in *Journal of the Atmospheric Sciences*. DOI 10.1175/JAS-D-23-0203.1.

drops with diameters > 40 μm are present, capable of initiating collision-coalescence. Some ice particles are detected at temperatures between -4 to -10 °C.

The ascent profile P2, occurring approximately 50 km further east, 45 minutes after P1 at 19.35 UTC during the return flight, may have coincidentally resampled air advecting east at 15 m s^{-1} from the P1 profile. The 0 °C level of 600-650 m within profile P2 is 100-150 m higher than at P1, while the cloud base has descended to ~ 800 m (Fig. 10d-f). Simultaneously the cloud top height has increased to 2.0-2.2 km altitude. A stable layer below the cloud base is consistent with melting-induced cooling. In this profile, N_d decreases from 600-650 cm^{-3} at cloud base to ~300 cm^{-3} near cloud top. Graupel coexists with super-cooled water at the upper levels, while larger snow aggregates are evident at temperatures slightly above 0 °C, transitioning to rain by the 5 °C temperature of the MinAlt leg (Fig. 9e, middle three images). The MinAlt leg-mean rainrate is relatively high at almost 0.5 mm hr^{-1}. Buoyancy fluxes exceed 500 W m^{-2} east of profile P2 (Fig. 2h) supporting 1Hz updrafts in the ACB leg that reach 5 m s^{-1}, for a leg-mean w of 3.5 m s^{-1}. The highest N_i of the 5 flight days, 2.5 L^{-1}, occurs near 0 °C (Fig. 9d, 19.15 UTC). 2DS imagery at 19.1 UTC indicates many ice (graupel) particles and snow aggregates of different sizes.

Further east by 50 km, the descent profile P3 at 18.8 UTC on the outgoing flight occurs just west of an open-celled cloud structure (Fig. 10g-i), wherein a BCT leg sampled a leg-mean N_i of 1.25 L^{-1} at a temperature of -10.5 °C. Large graupel and aggregates encountered at 18.8 UTC in Fig. 9b transition to rain by 18.83 UTC. The subsequent BCB leg samples aggregates and graupel at 1 °C (18.9 UTC, Fig. 9b) along with a leg-mean (liquid) rainrate of 0.25 mm hr^{-1}. N_i and IWC increase at cloud base, similar to P2.

Precipitation doesn't set in until the eastern GS edge, after which thick clouds transition into more open-celled structures. N_i also increases with fetch to the east. By then, the air near the surface is warm enough that snow aggregates melt into rain before reaching the surface (e.g., the 19.10 UTC BCB leg and 19.23 UTC MinAlt leg 2DS imagery in Fig. 9e). N_i is enhanced at both upper and lower cloud levels (see Fig. 10g in particular), summarized in Fig. 11. At upper levels (BCT temperatures ~ -10 °C), N_i increases with increasing LWC, with $N_{drizzle}$ (diameters > 40 μm), and with IWC (Fig. 11). Near or slightly below cloud base, at temperatures near 0 °C, the most pronounced dependence of N_i is with IWC (Fig. 11c).

Accepted for publication in *Journal of the Atmospheric Sciences.* DOI 10.1175/JAS-D-23-0203.1.

c. 3 February 2021 morning

Both planes reached the cloud transition region, after sampling thick stratiform cloud with maximum MODIS-derived LWPs > 200 g m^{-2} (Fig. 12). The stratiform cloud is visually the brightest of the 5 flight days (Fig. 2). Buoyancy fluxes exceeded 400 W m^{-2} at the western GS edge, corresponding to a 14 K air-sea temperature difference. The 1 Hz $w > 5$ m s^{-1} (Figs. 4 and S4) updrafts help support leg-mean $N_d > 700$ cm^{-3}. T_{ct} remain consistently near -10 °C, while cloud top heights simultaneously rise to over 2.5 km, the highest of the 5 flight days.

Five dropsondes, straddling the GS within 350 km and 2 hours of each other, detail the evolution of the boundary layer (Fig. 13). Furthest west (yellow, at 16.7 UTC), a well-mixed clear-air boundary layer of 1 km depth and a θ of 276 K overly an SST of ~ 286 K (Fig. 2). ~ 120 km further east (orange, near 15 TC)) the lower boundary layer θ has warmed by 2 K to 278 K, but the SSTs have increased even more, to ~ 294 K, so that the air-sea temperature difference has increased to 16 K, with the wind speeds also slightly stronger (Fig. 3) - in combination more than doubling the buoyancy flux (Fig. 3e). Interestingly, θ increases ~ 1 K within the lowest 200 m, despite the presence of snow (2DS image at 15.10 UTC in Fig. 12b) and a leg-mean rainrate of 0.26 mm hr^{-1} at 3 °C in the nearby MinAlt leg (Fig. 12c). Winds above the capping inversion shift from northeasterly to more easterly throughout.

Accepted for publication in *Journal of the Atmospheric Sciences.* DOI 10.1175/JAS-D-23-0203.1.

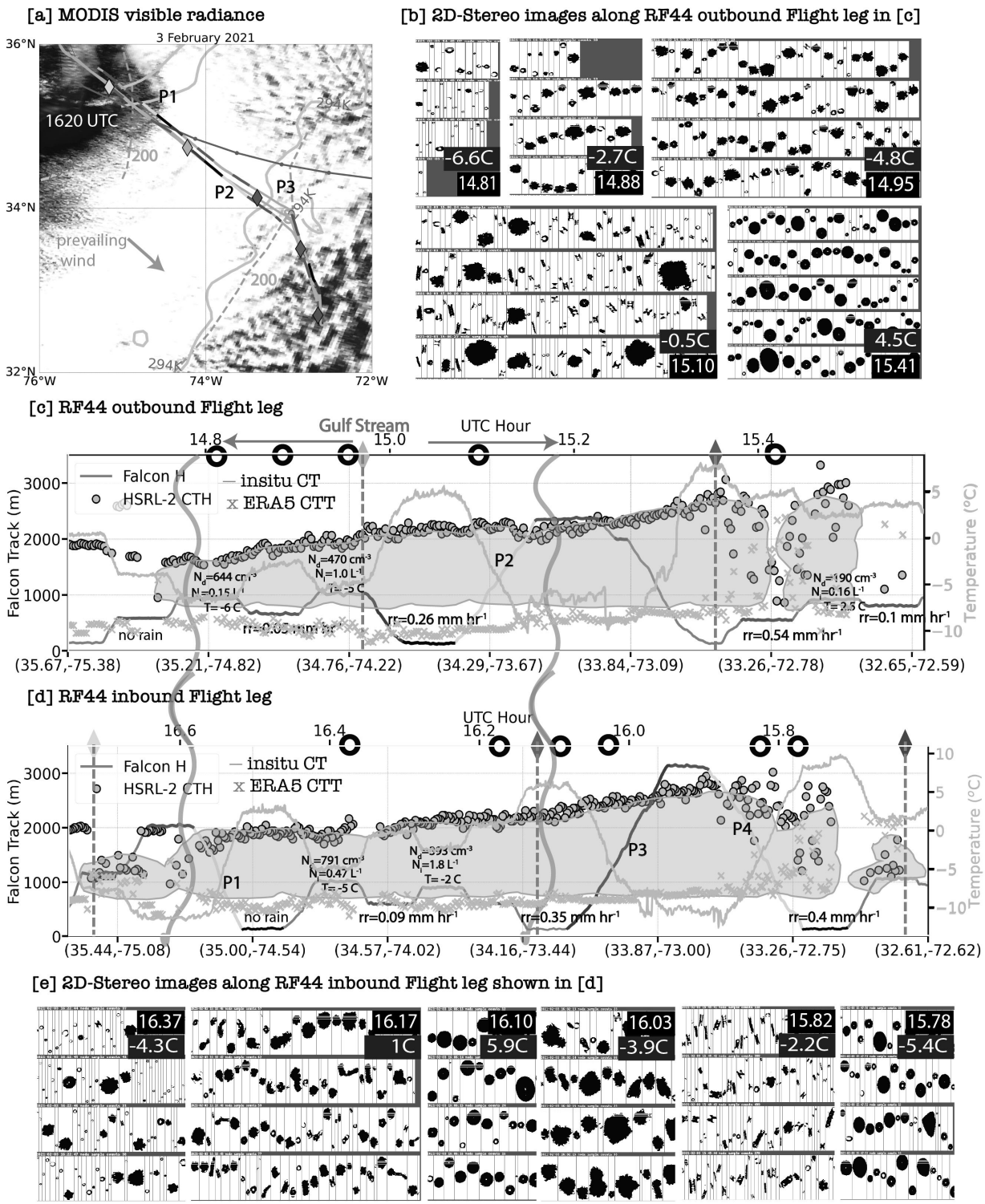

FIG. 12. 3 February 2021 morning (RF44). Similar notation to Fig. 5. FCDP cloud probe iced from 15.1 UTC until midway through P3 descent at 16.1 UTC (profiles shown in Fig. 14).

Accepted for publication in *Journal of the Atmospheric Sciences.* DOI 10.1175/JAS-D-23-0203.1.

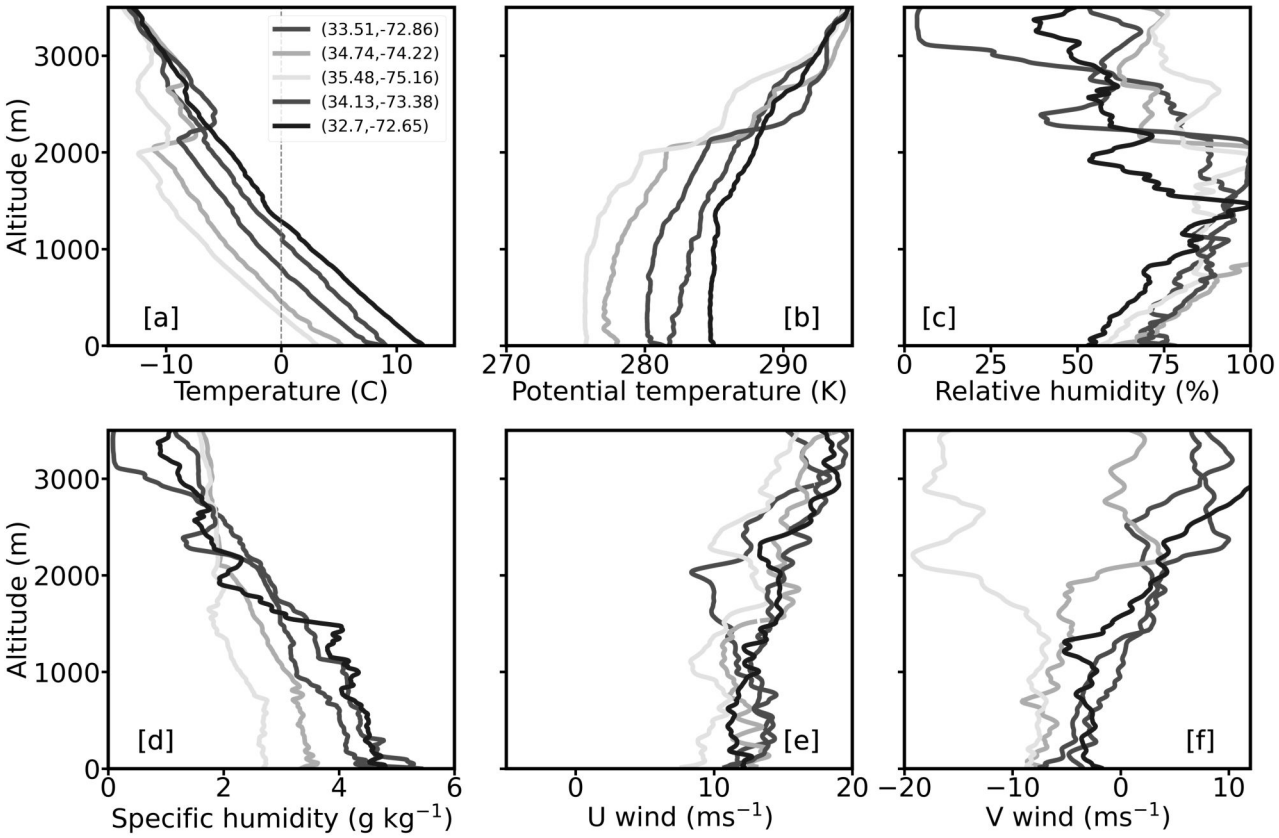

FIG. 13. 3 February 2021 morning (RF44) dropsonde profiles of a) temperature, b) potential temperature, c) relative humidity, d) specific humidity, e) zonal wind, and f) meridional winds. Colors follow the diamonds in Fig. 12: yellow dropsonde is west of the GS at 16.7 UTC, orange over the middle of the GS near 15 UTC, green at GS eastern edge near 16.1 UTC, red and blue just before and within the open-celled cloud structure at 15.35 UTC and 15.7 TC, respectively.

Accepted for publication in *Journal of the Atmospheric Sciences.* DOI 10.1175/JAS-D-23-0203.1.

At the eastern GS edge (green dropsonde, 16.1 UTC) the lower boundary layer has warmed to θ of 280 K in the lowest 1 km, despite near-surface rainrates of $\sim$ 0.35 mm hr $^{-1}$ (Fig. 12b). The lowest 100 m near the surface is nevetheless also warmer than the air above. Just before the transition to open-celled convection (red dropsonde, at 15.35 UTC), the boundary layer of approximately 2.5 km depth has incorporated a lower-tropospheric moist layer, helping to explain why this boundary layer is the deepest of the 5 days. The sub-cloud θ has warmed to 282 K, is overall more stably-stratified, and within the lowest 300 m, a cooling and moistening indicative of rain evaporation is now present, reflective of near-surface rainrates $>$ 0.5 mm hr^{-1} at 15.4 UTC,. Further east, within open-celled convection, a well-mixed, warmer (θ of 285 K), and moister boundary layer is now topped by a new inversion at 1.5 km. Air-sea temperature differences are still significant at 9 K, but combined with slightly diminished near-surface wind speeds of 10-12 m s^{-1}, the buoyancy fluxes have reduced to $<$ 200 W m^{-2} (Fig. 2- 3).

Interpreted together, the dropsondes indicate the 0 °C level increases from approximately 0.5 km to 1.2 km over a distance of $\sim$ 350 km (Fig. 13a), while simultaneously, the cloud base height descends towards the east (see ACB legs in Fig. 12). The cloud base temperatures increase from $\sim$ -4 °C to $\sim$ 3 °C with fetch. The boundary layer deepens, but loses its clear capping temperature inversion by the eastern GS edge. Precipitation increases to the east, reaching a maximum just prior to the transition to a more open-celled cloud morphology. Ice columns and snow aggregates are present in the overlying cloud (Fig. 12d, 2DS imagery at 14.95, 15.10, 15.82 and 16.03 UTC).

The 4 *in situ* profiles also indicate boundary layer deepening and a rising 0 °C level with fetch (Fig. 14). Rimed ice is again sampled during the first ACB leg, in thin cloud at a temperature of -6.6 °C (Fig. 12b, 14.81 UTC) and a leg-mean $N_d >$ 600 cm^{-3}. N_i increase as the clouds thicken, composed of ice columns and graupel, with supercooled liquid drops also present. The highest N_i occurs where drops with diameters $>$ 40 μm are most plentiful (15.1 UTC in Fig. 14, bottom row). N_i also increases with IWC in the ACB level legs (not shown). *In situ* BCT r_e are $\leq$ 10 μm, matched well by the RSP-retrieved r_e (Fig. A4c-d). The RSP retrievals indicate a small but consistent increase in cloud-top r_e with distance offshore (Fig. A4c-d). The RSP-derived LWP of 400 g m^{-2} increases over the thickest stratiform segment to LWPs $>$ 600 g m^{-2}, approximately matched by the profile LWPs (Fig. 14) and consistent with cloud deepening.

Accepted for publication in *Journal of the Atmospheric Sciences.* DOI 10.1175/JAS-D-23-0203.1.

d. 5 and 8 March 2021

By 5 March 2021, warmer GS waters extend further northeast (Fig. 2) but buoyancy fluxes, wind speeds, MODIS LWPs and maximum leg-mean N_d are all less than on 3 February 2021. Dropsonde profiles (7 total, Fig. S3) show a well-mixed boundary layer at the furthest west (19.82 UTC) capped at ~ 1.4 km, deepening to ~ 2.2 km by the eastern end. This corresponds to a cloud top rise of ~ 200 m per degree longitude. T_{ct} nevertheless warms slightly from ~ -10 °C to -8 °C. The 0 °C level rises from ~ 300 m to 1.1 km, although the cloud base always remains ≤ 0 °C (Fig. 15).

Similar to other flights, rimed ice particles are encountered on the first ACB leg (14.25 UTC, Fig. 15b) at *in situ* temperatures of -6 to -7 °C, within thin clouds with a minimum T_{ct} near -8 °C and N_d of ~ 400 cm^{-3}. 2DS imagery throughout depicts super-cooled liquid water droplets, occasional large rimed ice particles, and snow aggregates (e.g. 14.75, 15.11 and 15.46 UTC). The highest N_i of 0.58 L^{-1} is sampled during the furthest east BCT leg at 15.8 UTC at a temperature of -10 °C. Most particles near the melting level are ice (e.g. 14.88 UTC, Fig. 15b). The light rain present furthest east (15.04 UTC, Fig. 15e) is likely from melting snow, rather than collision-coalescence. The *in situ* profiles, though spanning cloud depths of almost 1 km, do not show much condensate (Fig. S5). Overall precipitation remains light (0.1 mm hr^{-1} at best) despite significant cloud deepening to the east. MODIS imagery does not clearly indicate an open-celled structure at the end of the morning or afternoon flight (Fig. 2), and the cloud thinning may simply result from entrainment of the drier air aloft.

Cloud thinning through entrainment can also explain the cloud dissipation with fetch on 8 March 2021 (Fig. S6). MODIS LWPs remain below 50 g m^{-2}, and in contrast to the other flights, clouds do not develop until the boundary layer flow reaches the eastern GS edge, after which they become more broken. The cloud base remains relatively high at 1.1-1.5 km. Unusual amongst the flights, no precipitation is detected anywhere below cloud base, and no particles qualify as ice (Fig. S7), although T_{ct} reach -5 °C. N_d does reduce by ~50% with fetch.

Accepted for publication in *Journal of the Atmospheric Sciences.* DOI 10.1175/JAS-D-23-0203.1.

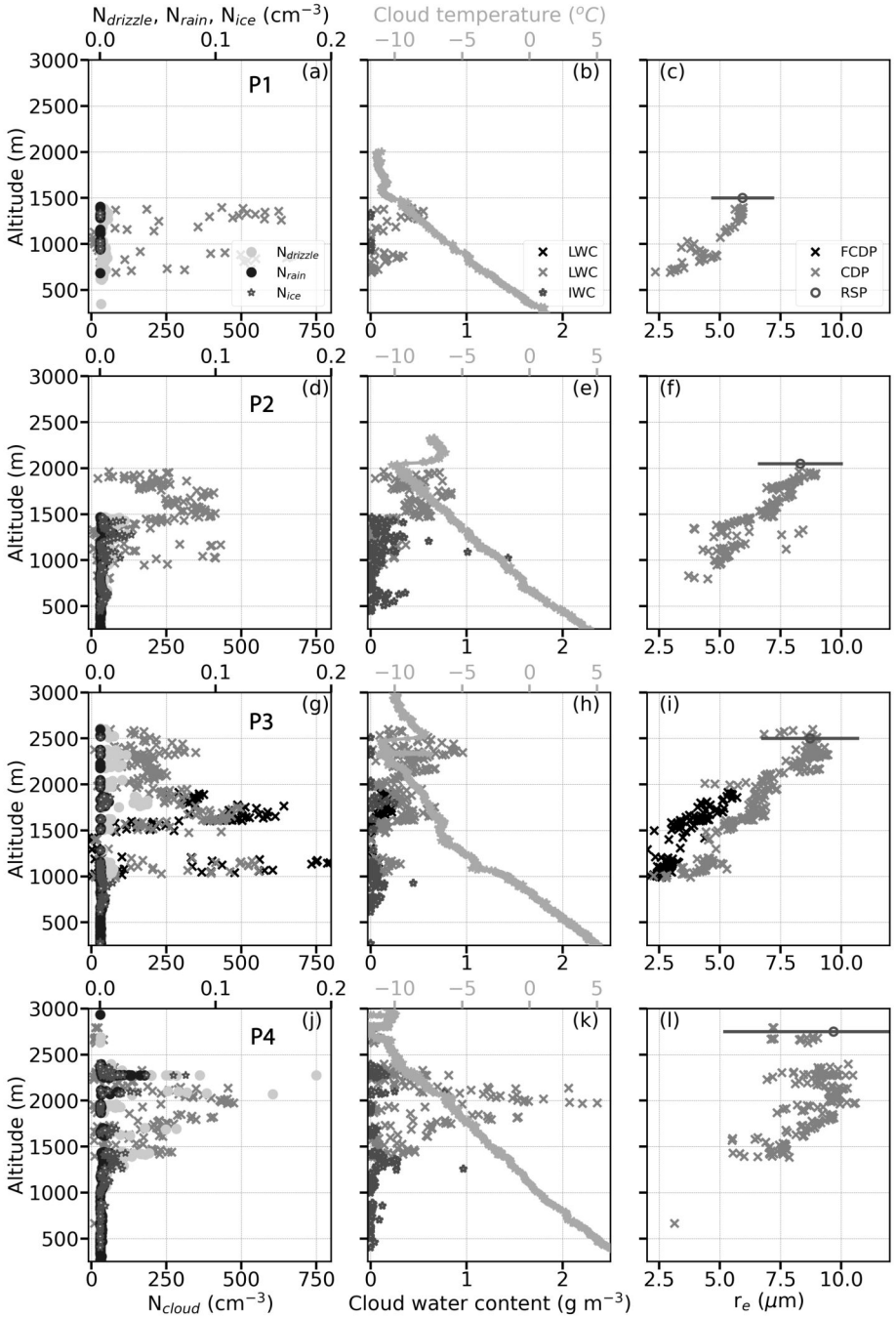

FIG. 14. Four *in situ* profiles from 3 February 2021 morning flight (RF44), organized from west (top) to east (bottom). FCDP (black asterisks in g)-i)) was iced but for a portion of the P3 descent. a)-c): P1 ascent at 16.55 UTC at 35.11°N, 74.67°W on the return (inbound) leg (CDP LWP=297 g m^{-2}). d)-f): P2 ascent at 15.1 UTC, 34.27°N, 73.65°W during outbound leg (LWP=526 g m^{-2}). g)-i): P3 descent at 15.95 UTC, 33.91°N, 73.07°W, on return (inbound) leg (LWP=400 g m^{-2}). j)-l): P4 ascent at 15.8 UTC, 33.36°N, 72.80°W, on return leg (LWP=95 g m^{-2}). Same labeling conventions as in Fig. 6. LWPs based on corrected CDP data.

Accepted for publication in *Journal of the Atmospheric Sciences.* DOI 10.1175/JAS-D-23-0203.1.

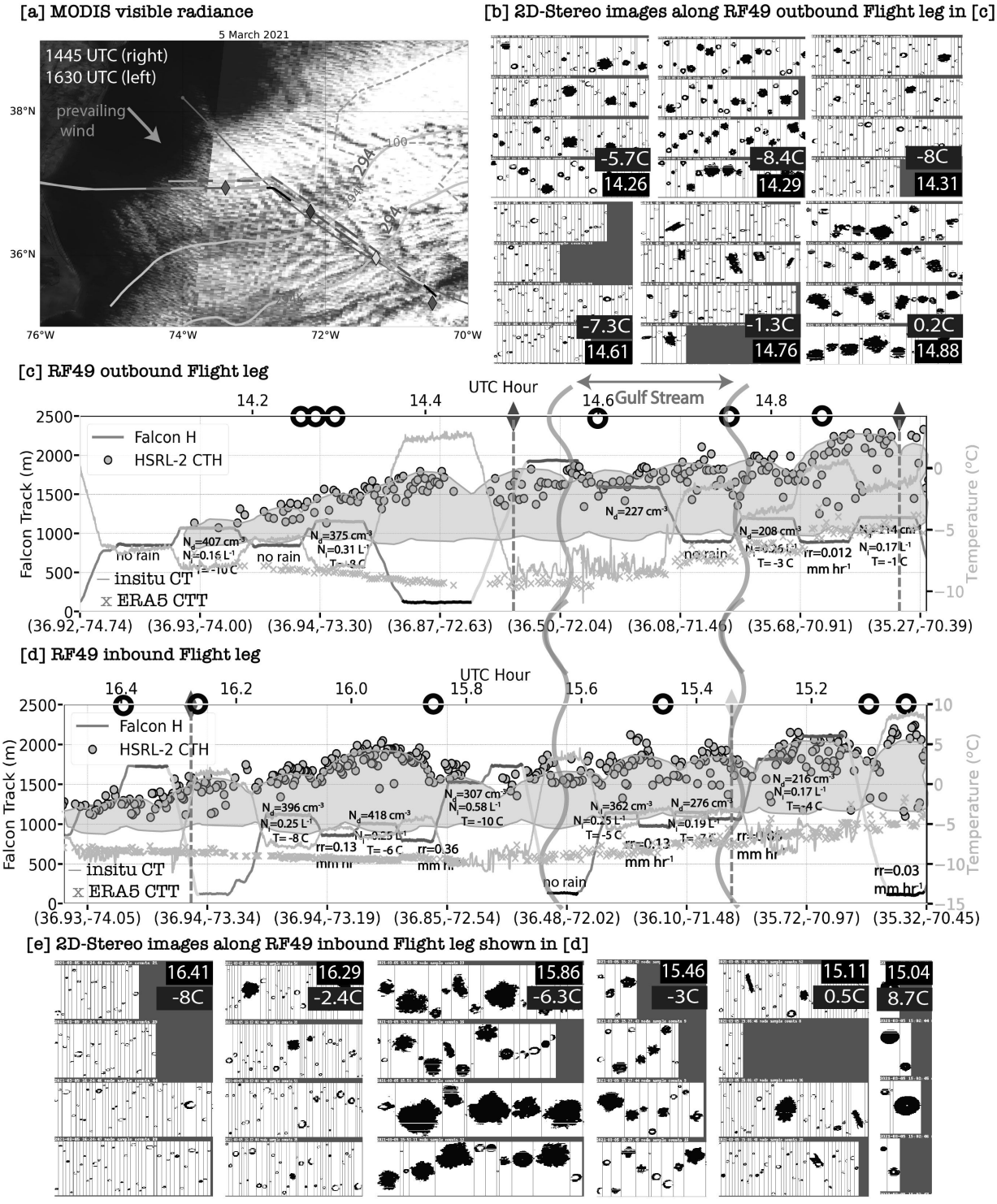

FIG. 15. 5 March 2021 morning (RF49). Similar notation to Fig. 5. First and third ascent partial profiles upon return shown in Fig. S5.

Accepted for publication in *Journal of the Atmospheric Sciences.* DOI 10.1175/JAS-D-23-0203.1.

5. Discussion

a. What Primary and Secondary Ice Production Processes are Occurring?

(Rimed) ice particles are detected during the first pass through thin, developing cloud, in 4 of the examined cases, at T_{ct} > -8 °C. The ice particles may have advected in from further upstream, and/or been brought down from the free troposphere. The small drop sizes (cloud top r_e < 10 μm) discourage splintering, and the proximity to clear sky upstream suggests primary ice nucleation may have occurred. The nucleation may be aided by high aerosol loadings within strong updrafts although the free troposphere is another potential source of INPs.

Nevertheless the N_i concentrations are often difficult to explain by primary ice production alone. At -10 °C, the Meyers et al. (1997) contact nucleation formulation estimates INP of 0.3 L^{-1} and the deposition freezing parameterization of Cooper (1986) produces an INP estimate of 0.05 L^{-1}. INP concentration estimates from other marine boundary layers containing dust remain well below 0.01 L^{-1} (Irish et al. 2019; Welti et al. 2020). Instead, measured N_i concentrations in these CAO clouds range from 0.1 L^{-1} to 5 L^{-1}, well above accepted INP values for temperatures > -15 °C.

Up- and downdrafts will distort the relationship between ice-originating temperatures and ice particle properties. The context in which ice particles are observed nevertheless help inform on potential ice production processes. Although the small sample size discourages robust statistics, larger N_i values occur both near colder cloud tops (< -8 °C) and warmer cloud bases (Fig. 16), and correlate with IWC for the three more intense CAOs (Fig. 17a). IWCs are higher for larger MODIS LWPs and cloud-top r_e (Fig. 17b and c), with a less clear relationship to the *in situ* r_e. Colder T_{ct} correspond to thicker clouds with more liquid water (Fig. S8, also noted by Tornow et al. (2023)), and the highest IWCs occur within the clouds with the coldest ERA5-determined T_{ct} (Fig. S9). These reach temperatures that favor dendritic vapor-diffusional growth whose slower particle fall speeds also allow more time for particle growth.

The best-known SIP mechanism, of rime-splintering at temperatures between -8 °C and -3 °C (Hallett and Mossop 1974) is evident in columns, super-cooled liquid drops, and rimed particles on 3 February 2021 (Fig. 12). Small ice columns are not always evident, however, such as within the strongest CAO occurring on 29 January 2021. The higher N_i associated with higher IWCs (Fig. 11) may indicate fragmentation after ice-ice particle collision, most effective at temperatures ~ -16 °C

Accepted for publication in *Journal of the Atmospheric Sciences.* DOI 10.1175/JAS-D-23-0203.1.

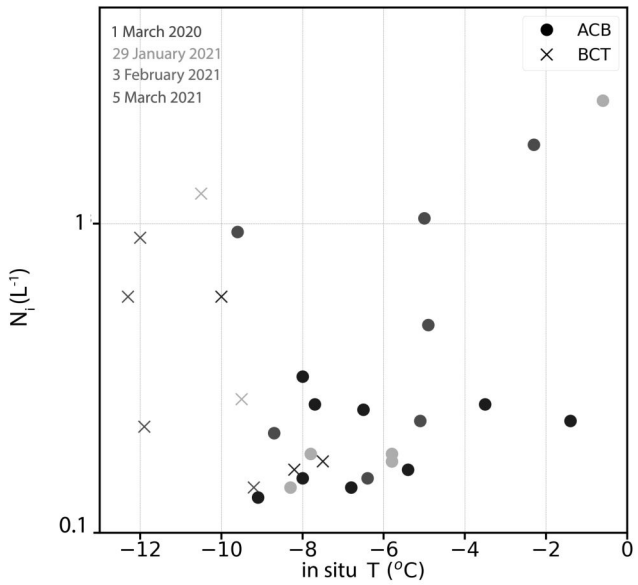

FIG. 16. Leg-mean *in-situ* N_i (one-second values > 0 only) versus temperature for the ACB (filled circles) and BCT (crosses) aircraft legs.

(Takahashi et al. 1995), or after ice aggregation near the 0° level. Recirculation of ice, facilitated by strong up/downdrafts, may facilitate a synergism across these SIP mechanisms (Sotiropoulou et al. 2020). Differences in riming fraction encourage a range of fall velocities that support further collisions (Korolev et al. 2020). The higher N_d and small r_e of these ACTIVATE CAOs should discourage droplet fragmentation upon freezing (drop-shattering), which is more likely for drop diameters > 100 μm (Korolev et al. 2020; Luke et al. 2021). Fragmentation through sublimation is also unlikely because the large number of super-cooled droplets will maintain a relative humidity near water-saturation.

b. Is Precipitation-Induced Decoupling Occurring?

Precipitation-induced decoupling is necessary to the transition to open-celled structures in sub-tropical marine stratocumulus (Wood et al. 2011), and is emphasized within Abel et al. (2017) for a sub-Arctic CAO cloud transition. We investigate boundary layer decoupling for the ACTIVATE CAOs using the metric developed within Jones et al. (2011), also applied within Abel et al. (2017). Differences between the upper (”top”) and lower (”bottom”) quarter of the boundary layer total water (ice+liquid+vapor mixing ratio; q_t) and the ice-liquid water potential temperature (θ_{il}) indicate the degree to which the cloud and sub-cloud layers are coupled. Profiles with Δq_t (=

Accepted for publication in *Journal of the Atmospheric Sciences.* DOI 10.1175/JAS-D-23-0203.1.

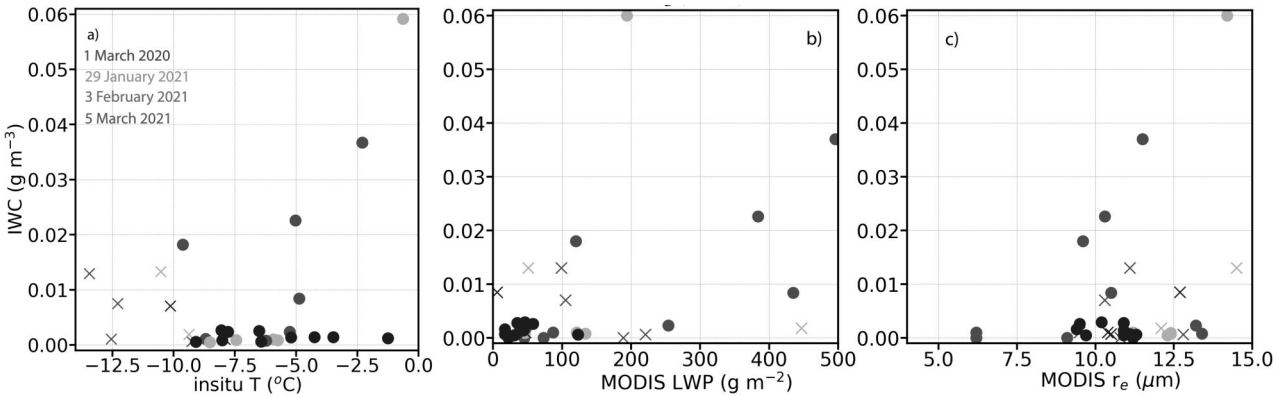

FIG. 17. Leg-mean *in-situ* IWC versus a) *in-situ* temperature, MODIS-derived b) LWP and c) cloud-top r_e, for above-cloud-base (ACB, filled circle) and below-cloud-top (BCT, crosses) aircraft legs. One-second N_i values > 0 only.

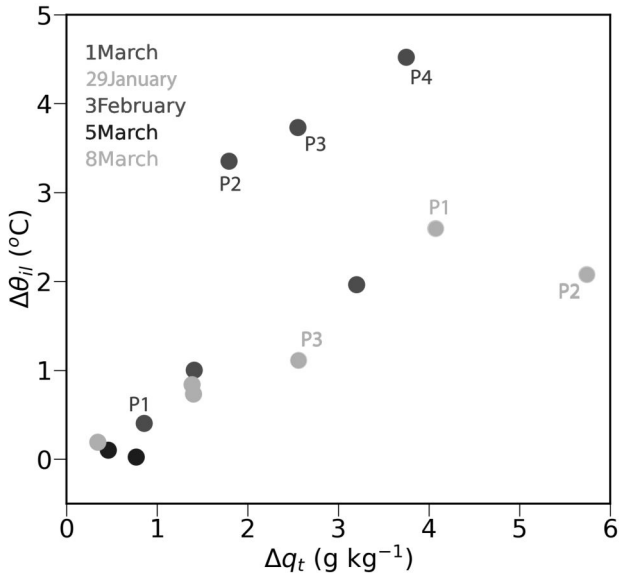

FIG. 18. Boundary layer decoupling metrics $\Delta\theta_{il}$ vs Δq_t. Profile labeling corresponds to that in Figs. 9-12 and Fig. 14.

$q_{t,bottom} - q_{t,top}$) of 1.5 g kg^{-1} and $\Delta\theta_{il}$ (= $\Delta\theta_{il,top} - \theta_{il,bottom}$) of $\simeq 1\ ^{\circ}C$ in Fig. 18 are considered well-mixed. These primarily occur on 5 and 8 March 2021 and the most western profiles from 1 March 2020 and 3 February 2021, supporting the inference that the cloud fraction on 5 and 8 March 2021 becomes reduced when the boundary layer becomes dried through cloud-top entrainment. More dramatic vertical gradients in q_t and θ_{il} occur further east. The deepest boundary layer, on 3 February, which was also raining, is the most decoupled in temperature (Figs. 12-13). Interestingly,

Accepted for publication in *Journal of the Atmospheric Sciences*. DOI 10.1175/JAS-D-23-0203.1.

TABLE 3. Dates (research flight numbers) and key science points of each flight day.

Date (RF numbers)	major points
1 March 2020 (RF13, RF14)	T_{ct} ~ -12 °C, N_d ~ 400 cm^{-3}, dendrites, graupel, aggregates
	transition to open-celled structures preceeded by precipitation
29 January 2021 (RF42)	MODIS LWPs > 250 g m^{-2}, N_i ~ 2.5 K^{-1}-maximum of the 5 days
	transition to open-celled structures preceeded by precipitation
3 February 2021 (RF44)	T_{ct} ~ -10 °C, N_i >1 L^{-1}, 0.5 mm hr^{-1} rain, cloud top height ~ 2 km, brightest cloud
	transition to open-celled structures preceeded by precipitation
5 March 2021 (RF49, RF50)	light rainrates, significant cloud deepening, T_{ct} ~ -8 °C, N_d ~ 400 cm^{-3}
	cloud transition more consistent with cloud-top entrainment than precipitation
8 March 2021 (RF51)	lack of ice, T_{ct} ~ -5 °C, no precipitation, high cloud base
	cloud thinning consistent with warming-deepening

despite being decoupled, most of the 29 January 2021 and 3 February 2021 profiles correspond to visually overcast conditions. This may indicate condensate detrainment near cloud-top.

6. Conclusions and Summary

As outbreaks of cold air flow off of the eastern north American continent in the boreal winter and spring over the cold Labrador current, and then over the warm Gulf Stream, strong surface fluxes of heat and moisture deepen the boundary layer, saturate its upper level with moisture and foster significant cloud development, over a distance of under 1000 km. The mid-latitude CAOs can include both rain and ice. The surface fluxes typically initiate cloud near the western GS edge at < 0 °C air temperatures, developing reflective stratiform cloud decks that devolve into lower-albedo cloud structures as the flow moves past the eastern GS edge. In the cases examined, cloud tops rise but mostly maintain their initial temperature, between -10 °C to -14 °C for the more intense CAOs. The cloud deepening and N_d depletion lag the SST increase, also noted in Tornow et al. (2022). The 0 °C level simultaneously rises while the cloud base descends and warms, by ~ 7K, so that more and more of the cloud comes to occupy above-freezing temperatures. Rain reaches the surface by the eastern GS edge, aided by melting of snow and graupel. The rain facilitates the transition of the more intense CAOs to an open-celled structures. These key characteristics are depicted in Fig. 19, with Table 3 summarizing the main points of each flight.

The CAOs occurring earlier in the year deepen more and sustain more ice and rain by the eastern GS edge, than do the less intense CAOs occurring later in the year, also documented within Painemal et al. (2023). The impact of the sub-seasonal trend in surface fluxes on the cloudy

Accepted for publication in *Journal of the Atmospheric Sciences*. DOI 10.1175/JAS-D-23-0203.1.

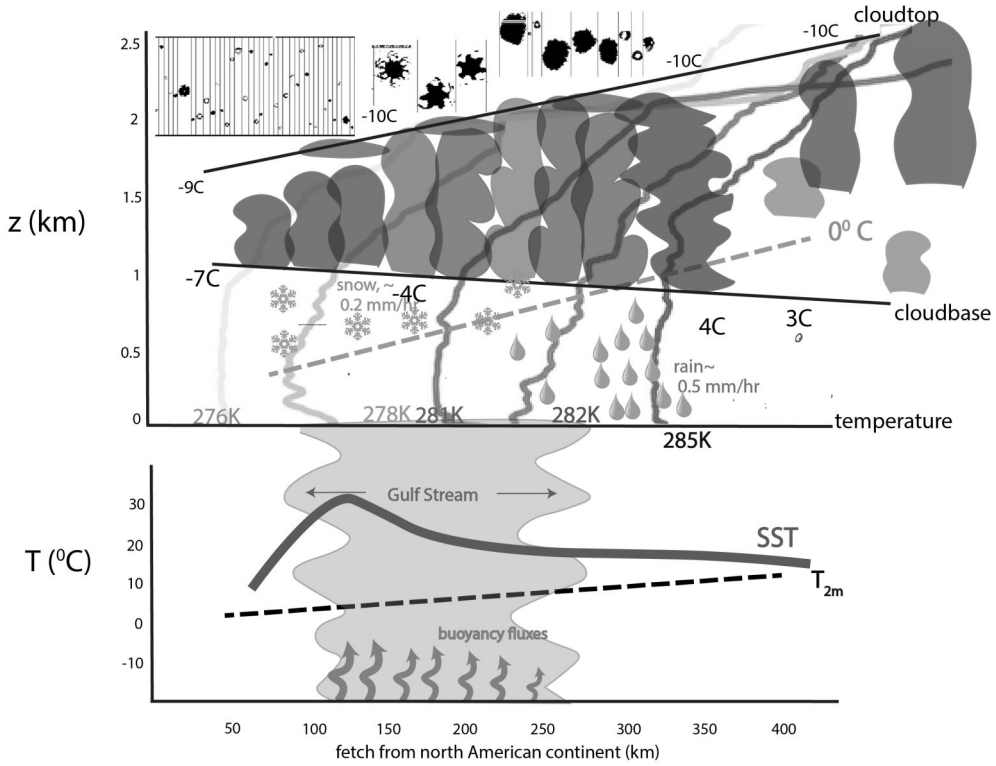

FIG. 19. Schematic depiction of main processes controlling the microphysical evolution of cold-air outbreaks over the northwest Atlantic, including the dropsonde profiles of potential temperature from 3 February 2021. Empirically, a cloud-top temperature of -10 °C generates an INP concentration of 0.0011 L^{-1} (Welti et al. 2020).

boundary layer is similar to the impact of latitudinal variations in Tornow et al. (2023). The weaker CAOs on 5 and 8 March 2021 have little or no precipitation and their cloud thinning and breakup is better explained by entrainment of drier air from above at cloud top.

Ice production is extensive. Ice is already present in thin, polluted clouds with small drops for which T_{ct} barely reaches -5 °C - -8 °C. We hypothesize the land-originating aerosol already contain some ice-nucleating particles, similar to measurements above Baffin Bay (Irish et al. 2019), with marine emissions a less significant source of INPs (DeMott et al. 2016; Creamean et al. 2022; Haëck et al. 2023). Strong updrafts, reaching 5 m s^{-1}, may aid ice nucleation (Kanji et al. 2017). The cold-air outbreaks examined here differ from those in the sub-Arctic and southern Ocean in part by being more polluted (Dadashazar et al. 2021), increasing the initial N_d to values > 500 cm^{-3}. Other studies document that more intense and polluted CAOs produce more extended high cloud fractions (Fletcher et al. 2016; Murray-Watson et al. 2023). After the initial icing, rimed ice co-exists with small supercooled liquid drops. In temperature ranges that favor dendritic growth,

Accepted for publication in *Journal of the Atmospheric Sciences.* DOI 10.1175/JAS-D-23-0203.1.

snowflakes are apparent (e.g. 1 March 2020). Updrafts and high aerosol loadings maintain small liquid drop sizes, influencing which SIP processes are more likely. These include ice-ice (including graupel) collisions favored in temperature ranges that support dendritic growth and enhanced ice aggregation, as well as Hallett-Mossop rime-splintering. Recirculation of ice within up- and downdrafts should support multiple SIP pathways, similar to the sub-Arctic (Sotiropoulou et al. 2020; Karalis et al. 2022) and over the southern Oceans (Järvinen et al. 2022). Small drop sizes should discourage droplet freezing, all else equal. The N_i enhancement is consistent with other high-latitude measurements within convective clouds at T_{ct} > -12 °C (Abel et al. 2017; Field et al. 2017; Zaremba et al. 2021), although the surface fluxes and updrafts over this western boundary current domain are stronger, and also help explain a positive coassociation between LWP and N_d not seen in other regions (Gryspeerdt et al. 2019).

Counterintuitively, INP parameterizations applied within global models (Bigg 1953; Cooper 1986; Meyers et al. 1997), overestimate INPs relative to measurements by 1-2 orders of magnitude at the temperatures spanning ACTIVATE CAOs (Irish et al. 2019; Welti et al. 2020). This places emphasis on improving model representations of SIP processes (Atlas et al. 2022). More work is also needed to better assess the various remote sensor retrievals in these mixed-phase conditions (see Appendix for a preliminary analysis). Mesoscale wind circulations generated either by the strong SST gradients (Small et al. 2008; Liu et al. 2014) or above-cloud-top wind shear (Young et al. 2002) may also impose imprints on the cloud organization, but this remains a topic for future research.

Accepted for publication in *Journal of the Atmospheric Sciences.* DOI 10.1175/JAS-D-23-0203.1.

Acknowledgments. We gratefully acknowledge funding support through grant 80NSSC19K0390 to University of Miami and grant no. 80NSSC19K0442 to University of Arizona. Christiane Voigt and Simon Kirschler were funded by the Deutsche Forschungsgemeinschaft (DFG, German Research Foundation – TRR 301 – Project ID 428312742 and SPP 1294 HALO under contract no. VO 1504/79-1). We thank Kevin Sanchez and Alexei Korolev for their insights into cloud probe behavior and microphysical behavior. We are also grateful to the anonymous reviewers: their comments have improved the final paper. The NASA Earth Venture Suborbital-3 Aerosol Cloud meTeorology Interactions Ver the western ATlantic Experiment (ACTIVATE) campaign was funded by NASA's Earth Science Division and managed through the Earth System Science Pathfinder Program Office.

Author Contributions: PZ led the writing and direction, SC performed the analysis, SK, CV, BC, EC, RF, JH, TS, MS, KT contributed datasets and all authors contributed to the final writing.

Data availability statement. All ACTIVATE datasets are available through ASDC: Atmospheric Science Data Center [data set], `https://doi.org/10.5067/SUBORBITAL/ACTIVATE/DATA001`, 2020.

APPENDIX A

Assessment of *in situ* and remotely-retrieved cloud properties

CDP N_d values are typically smaller than those from the FCDP, but the r_e values are similar between the 2 probes for 2020 data, suggesting the N_d difference is primarily an undercounting at all sizes. In coincidence undercounting, 2 or more particles simultaneously travel through a sample volume but are counted as one. Differences in the effective flow speed of $\sim 15\%$ can further contribute to N_d differences. An empirical correction based on 2020 data corrects for the CDP coincidence undercounting: $N_{d,CDP_{corr}} = \alpha\ (e^{(\beta * N_{d,CDP})} - 1)$, with α=1820 and β =6.9e-4 (Kevin Sanchez, personal communication). This closely follows the Lance (2012) correction.

Small changes in voltage can also dramatically change the number of droplets meeting the 3 μm diameter threshold of the FCDP, however. FCDP N_d are typically only slightly less than the cloud condensation nuclei (CCN) concentrations measured at 0.3-0.4 % supersaturation (Fig. A1a) for the 5 investigated flight days. The (corrected) CDP N_d values relate more typically to the CCN

Accepted for publication in *Journal of the Atmospheric Sciences.* DOI 10.1175/JAS-D-23-0203.1.

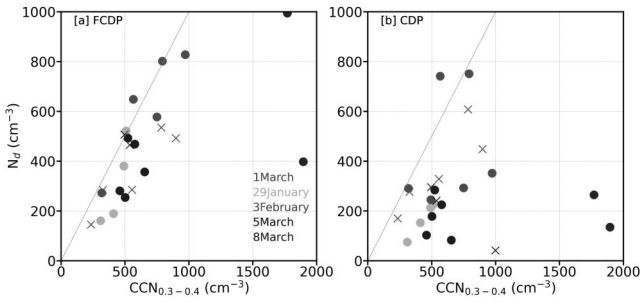

FIG. A1. N_d versus cloud condensation nuclei (*CCN*) concentration measured at 0.3-0.4% supersaturation, based on level legs occurring below 1 km gridded to 1°, for a) FCDP and b) the corrected CDP data.

values for marine environments. The FCDP N_d values, while high, are nevertheless possible for a regime with strong surface fluxes, and cannot be discounted.

The available remotely-retrieved (RSP, MODIS, and Advanced Microwave Scanning Radiometer-2 (AMSR2)) cloud properties are also compared to those calculated from the available *in situ* profiles, for both probes (Fig. A2- A3), and, for the RSP, compared to the CDP r_e along the 3 February 2021 flight track (Fig. A4). The RSP retrieves the r_e and cloud optical depth τ using multi-angle polarized radiances at the cloud bow, primarily at the 865 nm wavelength. The radiances are dominated by single scattering and little impacted by three-dimensional radiative transfer effects (Alexandrov et al. 2012, 2015). The data, at a native field of view resolution of 14 mrad, are first aggregated into a 1 Hz resolution (~ 100 m spatial resolution) oriented along the aircraft track, then into 1-minute moving averages (Fig. A4). The RSP r_e is typically within 2 μm of the *in situ* BCT values (Fig. A2b, Fig. A3b and Fig. S8) and slightly exceed the *in situ* values from lower in the cloud, as expected (Fig. A4e-f). A larger-scale assessment of ACTIVATE data (not shown) is similar, as are comparisons to Langley CDP data over the northern Atlantic (Alexandrov et al. 2018), and from another cloud probe over the southeast Atlantic (Adebiyi et al. 2020). In sum the comparison in Figs. A2-A4 supports both the *in situ* and RSP r_e characterizations.

In-situ cloud optical depth (τ) values are summed from regridded 20-m vertical-mean volume extinction coefficients ($\beta(z)$) calculated as $\beta(z) = \frac{9LWC}{5\rho_w r_e(z)}$. The factor of $\frac{9}{5}$ accounts for an adiabatic increase in LWC over the 20-m span, supported by the profiles. For the 6 *in situ* profiles for which RSP retrievals are also available, the RSP τ values are within sampling uncertainties. Differences from *in situ* LWP values are dominated by the differences in τ (LWP is estimated using $\frac{5}{9}\rho_w \tau r_e$ at cloudtop). RSP N_d retrievals, calculated from $N_d = k\frac{\tau^{0.5}}{r_e^{2.5}}$ with k=1.4067 x 10^{-6} [cm$^{-0.5}$] (Painemal

Accepted for publication in *Journal of the Atmospheric Sciences.* DOI 10.1175/JAS-D-23-0203.1.

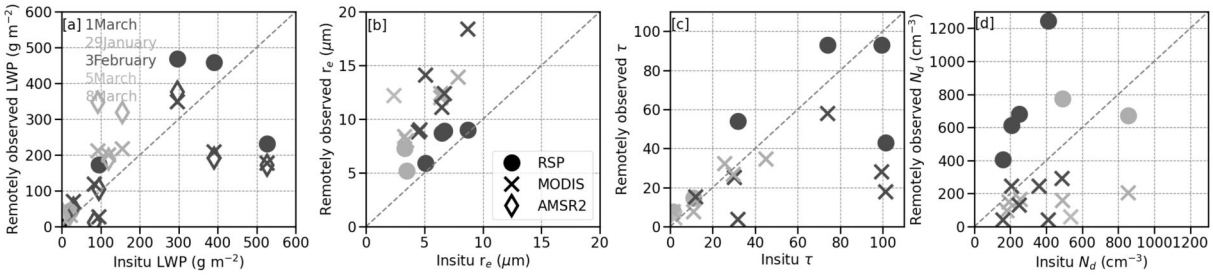

FIG. A2. RSP (filled circles) and MODIS (crosses) retrievals versus *in-situ* FCDP-derived values of a) LWP, includes microwave-derived AMSR2 (diamond), b) cloud-top r_e, c) cloud optical depth τ, and d) N_d. Flight day is indicated by color. RSP data are screened for the presence of higher clouds.

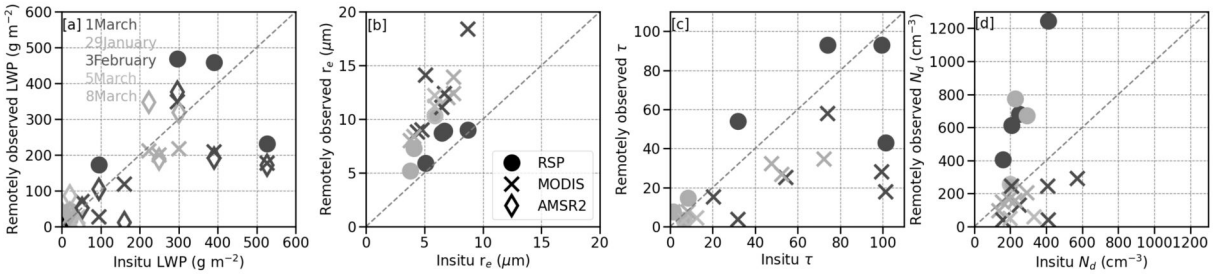

FIG. A3. similar to Fig. A2 but for CDP probe values.

and Zuidema 2011) typically exceed vertically-averaged *in situ* values, similar to Gryspeerdt et al. (2022). This does reflect *in situ* vertical inhomogeneity in part. Along the 3 February 2021 flight track, the RSP-derived N_d are close to the maximum *in situ* N_d values (Fig. A4g-h), reaching 1000 cm^{-3} in places, while retrieved LWPs mostly remain 500 g m^{-2}. These comparisons support each instrument's separate estimate.

MODIS r_e values, retrieved at 3.7 μm, typically exceed *in situ* values (see also Fig. S7), consistent with Painemal and Zuidema (2011); Painemal et al. (2021). MODIS τ are < *in situ* τ, consistent with unaccounted-for horizontal photon transport (Zuidema and Evans 1998). MODIS biases in τ and r_e compensate within the LWP estimate. MODIS LWPs are less than RSP-derived LWPs (Figs. A2a-A3a), in large part because of resolution differences (100 m from RSP versus 1 km for MODIS): RSP LWPs retrieved from the 1-minute RSP radiances are 60%-70% of the LWPs retrieved at the native resolution and thereafter averaged (Fig. A4). Fully-independent AMSR2 LWP estimates appear closer to the *in-situ* values (Figs. A2a and A3a), but this may be fortuitous, as the time differences are also larger. MODIS N_d values are consistently less than the vertically-

Accepted for publication in *Journal of the Atmospheric Sciences*. DOI 10.1175/JAS-D-23-0203.1.

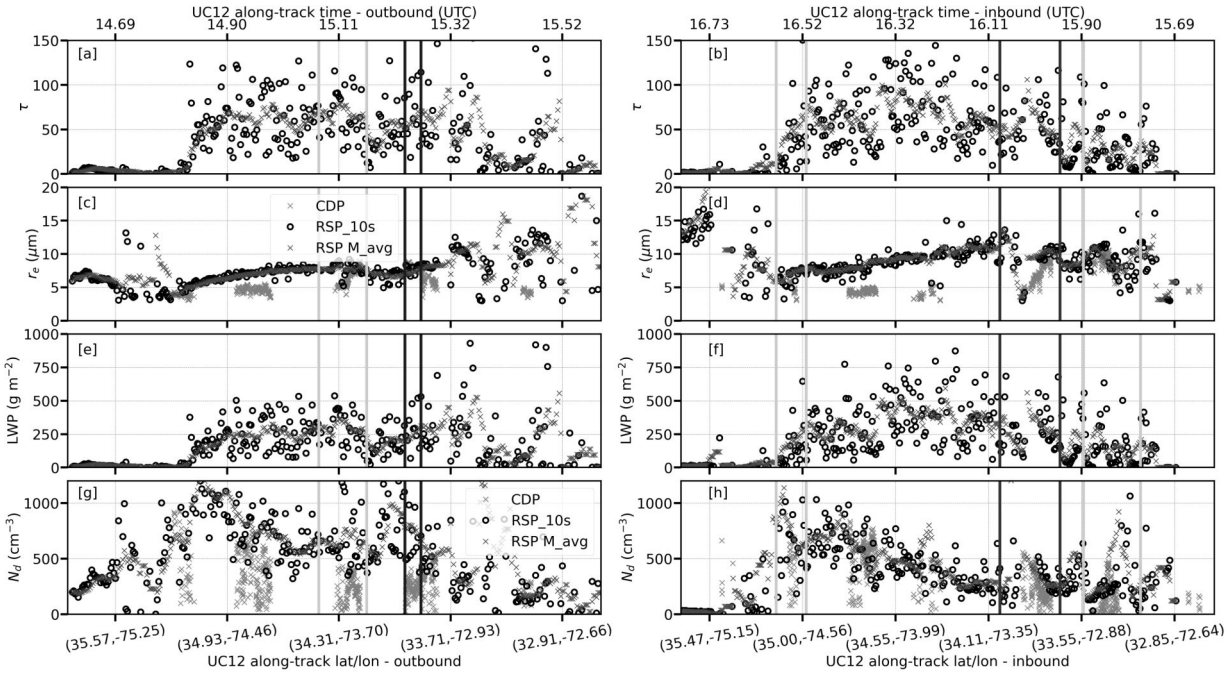

FIG. A4. a) RSP-derived cloud optical depths along outbound flight track of 3 February 2021 morning flight (RF44), from west to east, as 10-second and moving 1-minute averages (black open circles and red asterisks, respectively). b) same as a) but for inbound (return) flight, west to east. c)-d): same as a)-b) but for RSP-derived and CDP probe r_e where available (grey asterisks). e)-f): RSP-derived LWP. g)-h) RSP-derived and CDP probe N_d where available (grey asterisks). Yellow/purple lines bracket ascent/descent profiles and dark blue indicates the BCT leg.

averaged *in situ* values, also seen in (Gryspeerdt et al. 2022). We speculate this is because of the strong dependence on a biased MODIS r_e estimate.

References

Abel, S. J., I. A. Boutle, K. Waite, S. Fox, P. R. Brown, and R. C. et al., 2017: The role of precipitation in controlling the transition from stratocumulus to cumulus clouds in a northern hemisphere cold-air outbreak. *J. Atmos. Sci.*, **74**, 2293–2314, https://doi.org/10.1175/jas-d-16-0362.1.

Adebiyi, A. A., P. Zuidema, I. Chang, S. P. Burton, and B. Cairns, 2020: Mid-level clouds are frequent above the southeast atlantic stratocumulus clouds. *Atmos. Chem. Phys.*, **20**, 11 025–11 043, https://doi.org/10.5194/acp-20-11025-2020.

Accepted for publication in *Journal of the Atmospheric Sciences.* DOI 10.1175/JAS-D-23-0203.1.

Alexandrov, M., B. Cairns, A. Wasilewski, A. Ackerman, M. McGill, and e. a. J. Yorks, J., 2015: Liquid water cloud properties during the polarimeter definition experiment (PODEX). *Rem. Sens. Env.*, **169**, 20–36.

Alexandrov, M. D., B. Cairns, C. Emde, A. S. Ackerman, and B. van Diedenhoven, 2012: Accuracy assessments of cloud droplet size retrievals from polarized reflectance measurements by the research scanning polarimeter. *Rem. Sens. Env.*, **125**, 92–111.

Alexandrov, M. D., and Coauthors, 2018: Retrievals of cloud droplet size from the research scanning polarimeter data: Validation using in situ measurements. *Remote Sens. Environ.*, **210**, 76–95, https://doi.org/10.1016/j.rse.2018.03.005.

Atlas, R. L., C. S. Bretherton, M. F. Khairoutdinov, and P. N. Blossey, 2022: Hallett-mossop rime splintering dims cumulus clouds over the southern ocean: New insight from nudged global storm-resolving simulations. *AGU Advances*, **3**, https://doi.org/10.1029/2021AV000454.

Baker, B., and R. P. Lawson, 2006: Improvement in determination of ice water content from two-dimensional particle imagery. part i: Image-to-mass relationships. *J. Appl. Meteor. Clim.*, **45**, 1282–1290.

Bigg, E. K., 1953: The supercooling of water. *Proc. Phys. Soc.*, **66B**, 688–694, https://doi.org/10.1088/0370-1301/66/8/309.

Cooper, W. A., 1986: Ice initiation in natural clouds. *Precipitation Enhancement—A Scientific Challenge, Meteor. Monogr.*, 29–32.

Corral, A. F., and Coauthors, 2021: An overview of atmospheric features over the Western North Atlantic Ocean and North American East Coast – Part 1: Analysis of aerosols, gases, and wet deposition chemistry. *J. Geophys. Res.*, **126**, https://doi.org/10.1029/2020JD032592.

Creamean, J. M., and Coauthors, 2022: Annual cycle observations of aerosols capable of ice formation in central Arctic clouds. *Nat. Commun.*, **13**, 3537–3549.

Dadashazar, H., and Coauthors, 2021: Cloud drop number concentrations over the western north atlantic ocean: Seasonal cycle, aerosol interrelationships, and other influential factors. *Atmos. Chem. Phys.*, **21**, 10 499–10 526, https://doi.org/10.5194/acp-21-10499-2021.

Accepted for publication in *Journal of the Atmospheric Sciences.* DOI 10.1175/JAS-D-23-0203.1.

DeMott, P. J., T. Hill, C. McCluskey, K. Prather, D. Collins, and R. S. et al., 2016: Sea spray aerosol as a unique source of ice nucleating particles. *PNAS*, **113**, 5797–5803.

Field, P. R., and A. J. Heymsfield, 2015: Importance of snow to global precipitation. *Geophys. Res. Lett.*, **42**, 9512–9520, https://doi.org/10.1002/2015GL065497.

Field, P. R., and Coauthors, 2017: Exploring the convective grey zone with regional simulations of a cold air outbreak. *Q.J.R. Meteorol. Soc*, **143**, 2537–2555, https://doi.org/10.1002/qj.3105.

Fletcher, J. K., S. L. Mason, and C. Jakob, 2016: A climatology of clouds in marine cold air outbreaks in both hemispheres. *J. Climate*, **29**, 6677–6692, https://doi.org/10.1175/JCLI-D-15-0783.1.

Geerts, B., and Coauthors, 2022: The COMBLE Campaign: A Study of Marine Boundary Layer Clouds in Arctic Cold-Air Outbreaks. *Bull. Am. Meteor. Soc.*, **103 (5)**, E1371 – E1389, https://doi.org/10.1175/BAMS-D-21-0044.1.

Gryspeerdt, E., and Coauthors, 2019: Constraining the aerosol influence on cloud liquid water path. *Atmos. Chem. Phys.*, **19**, 5331–5347.

Gryspeerdt, E., and Coauthors, 2022: The impact of sampling strategy on the cloud droplet number concentration estimated from satellite data. *Atmos. Meas. Tech.*, **15**, 3875–3892, https://doi.org/10.5194/amt-15-3875-2022.

Hallett, J., and S. C. Mossop, 1974: Production of secondary ice particles during the riming process. *Nature*, **249**, 26–28, https://doi.org/10.1038/249026a0.

Haëck, C., M. Lévy, I. Mangolte, and L. Bopp, 2023: Satellite data reveal earlier and stronger phytoplankton blooms over fronts in the gulf stream region. *Biogeosciences*, **20**, 1741–1758.

Hu, Y., and Coauthors, 2009: CALIPSO/CALIOP Cloud Phase Discrimination Algorithm. *J. Atmos. and Ocean. Tech.*, **26**, 2293–2309, https://doi.org/https://doi.org/10.1175/2009JTECHA1280.1.

Irish, V. E., and Coauthors, 2019: Ice nucleating particles in the marine boundary layer in the canadian arctic during summer 2014. *Atmos. Chem. Phys.*, **19**, 1027–1039.

Jonas, P. R., 1996: Turbulence and cloud microphysics. *Atmos. Res.*, **40**, 283–306.

Accepted for publication in *Journal of the Atmospheric Sciences*. DOI 10.1175/JAS-D-23-0203.1.

Jones, C. R., C. S. Bretherton, and D. Leon, 2011: Coupled vs. decoupled boundary layers in VOCALS-REx. *Atmos. Chem. Phys.*, 7143–7153, https://doi.org/10.5194/acp-11-7143-2011.

Järvinen, E., and Coauthors, 2022: Evidence for secondary ice production in southern ocean maritime boundary layer clouds. *J. Geophys. Res.*, **127**.

Kanji, Z. A., L. A. Ladino, H. Wex, Y. Boose, M. Burkert-Kohn, D. J. Cziczo, and M. Kr¨amer, 2017: Overview of ice nucleating particles. ice formation and evolution in clouds and precipitation: Measurement and modeling challenges. *Meteor. Monogr.*, **No. 58**.

Karalis, M., G. Sotiropoulou, S. J. Abel, E. Bossioli, P. Georgakaki, G. Methymaki, A. Nenes, and M. Tombrou, 2022: Effects of secondary ice processes on a stratocumulus to cumulus transition during a cold-air outbreak. *Atmos. Res.*, **277**, https://doi.org/https://doi.org/10.1016/j.atmosres.2022.106302.

Kirschler, S., and Coauthors, 2022: Seasonal updraft speeds change cloud droplet number concentrations in low-level clouds over the western north atlantic. *Atmos. Chem. Phys.*, **22**, 8299–8319, https://doi.org/10.5194/acp-22-8299-2022.

Kirschler, S., and Coauthors, 2023: Overview and statistical analysis of boundary layer clouds and precipitation over the western north-atlantic ocean. *Atmos. Chem. Phys. Disc.*, https://doi.org/10.5194/egusphere-2023-898.

Korolev, A., and Coauthors, 2020: A new look at the environmental conditions favorable to secondary ice production. *Atmos. Chem. Phys.*, **20**, 1391–1429, https://doi.org/10.5194/acp-20-1391-2020.

Korolev, A. V., J. W. Strapp, and G. A. Isaac, 1998: Evaluation of the accuracy of PMS Optical Array Probes. *J. Atmos. Oc. Tech.*, **15**, 708–720.

Lance, S., 2012: Coincidence errors in a Cloud Droplet Probe (CDP) and a Cloud and Aerosol Spectrometer (CAS), and the Improved Performance of a Modified CDP. *J. Atmos. Oceanic Tech.*, **29**, 1532–1541, https://doi.org/10.1175/JTECH-D-11-00208.1.

Liu, J., S. Xie, J. R. Norris, and S. Zhang, 2014: Low-level cloud response to the gulf stream front in winter using CALIPSO. *J. Clim.*, **27**, 4421–4432.

Accepted for publication in *Journal of the Atmospheric Sciences.* DOI 10.1175/JAS-D-23-0203.1.

Luke, E. P., F. Yang, P. Kollias, A. Vogelmann, and M. Maahn, 2021: New insights into ice multiplication using remote-sensing observations of slightly supercooled mixedphase clouds in the arctic. *Proc. Natl. Acad. Sci.*, **118**, https://doi.org/10.1073/pnas.2021387118.

Matus, A. V., and T. S. L'Ecuyer, 2017: The role of cloud phase in earth's radiation budget. *J. Geophys. Res.*, **122**, 2559–2578, https://doi.org/10.1002/2016JD025951.

McCluskey, C. S., T. C. Hill, R. Humphries, A. Rauker, S. Moreau, and P. S. et al., 2018: Observations of ice nucleating particles over southern ocean waters. *Geophys. Res. Lett.*, **45**, 11 989–11 997, https://doi.org/10.1029/2018GL079981.

McFarquhar, G. M., C. S. Bretherton, R. Marchand, A. Protat, P. DeMott, and S. A. et al., 2021: Observations of clouds, aerosols, precipitation, and surface radiation over the southern ocean: An overview of CAPRICORN, MARCUS, MICRE and SOCRATES. *Bull. Am. Meteor. Soc.*, **102**, E894–E928, https://doi.org/10.1175/bams-d-20-0132.1.

Meyers, M. P., R. L. Walko, J. Y. Harrington, and W. R. Cotton, 1997: New RAMS cloud microphysics parameterization. Part II: The two-moment scheme. *Atmos. Res.*, **45**, 3–39.

Minobe, S., A. Kuwano-Yoshida, and N. K. et al., 2008: Influence of the gulf stream on the troposphere. *Nature*, **452**, 206–209, https://doi.org/10.1038/nature06690.

Mülmenstadt, J., O. Sourdeval, J. Delano, and J. Quaas, 2015: Frequency of occurrence of rain from liquid-, mixed-, and ice-phase clouds derived from A-Train satellite retrievals. *Geophys. Res. Lett.*, **42**, 6502–6509, https://doi.org/10.1002/2015GL064604.

Murray-Watson, R. J., E. Gryspeerdt, and T. Goren, 2023: Investigating the development of clouds within marine cold air outbreaks. *Atmos. Chem. Phys. Disc.*

Nakajima, T., and M. D. King, 1990: Determination of the optical thickness and effective particle radius of clouds from reflected solar radiation measurements. part i: Theory. *J. Atmos. Sci.*, **47**, 1878–1893.

Naud, C. M., J. F. Booth, K. Lamer, R. Marchand, A. Protat, and G. McFarquhar, 2020: On the relationship between the marine cold air outbreak m parameter and low-level cloud heights in the midlatitudes. *J. Geophys. Res.*, **125**, https://doi.org/10.1029/2020JD032465.

Accepted for publication in *Journal of the Atmospheric Sciences.* DOI 10.1175/JAS-D-23-0203.1.

Painemal, D., and P. Zuidema, 2011: Assessment of MODIS cloud effective radius and optical thickness retrievals over the Southeast Pacific with VOCALS-REx in-situ measurements. *J. Geophys. Res.*, **116**, https://doi.org/10.1029/2011JD016155.

Painemal, D., and Coauthors, 2021: Evaluation of satellite retrievals of liquid clouds from the GOES-13 imager and MODIS over the midlatitude North Atlantic during the NAAMES campaign. *Atmos. Meas. Tech.*, **14**, 6633–6646.

Painemal, D., and Coauthors, 2023: Wintertime synoptic patterns of variability of midlatitude boundary layer clouds over the western North Atlantic: Climatology and insights from in-situ ACTIVATE observations. *J. Geophys. Res.*, https://doi.org/10.1029/2022JD037725.

Papritz, L., S. Pfahl, H. Sodemann, and H. Wernli, 2015: A climatology of cold air outbreaks and their impact on air–sea heat fluxes in the high-latitude south pacific. *J. Climate*, **28**, 342–364, https://doi.org/10.1175/JCLI-D-14-00482.1.

Plagge, A., J. B. Edson, and D. Vandemark, 2016: In situ and satellite evaluation of air–sea flux variation near ocean temperature gradients. *J. Climate*, **29**, 1583–1602, https://doi.org/10.1175/jcli-d-15-0489.1.

Pruppacher, H. R., and J. D. Klett, 1997: Microphysics of clouds and precipitation. https://doi.org/10.1007/978-0-306-48100-0.

Seethala, C., and Coauthors, 2021: On assessing ERA5 and MERRA2 representations of cold-air outbreaks across the Gulf Stream. *Geophys. Res. Lett.*, **48**, https://doi.org/10.1029/2021GL094364.

Small, R. J., and Coauthors, 2008: Air-sea interaction over ocean fronts and eddies. *Dyn. Atmos. Oc.*, **45**, 274–319, https://doi.org/10.1016/j.dynatmoce.2008.01.001.

Sorooshian, A., and Coauthors, 2019: Aerosol-Cloud-Meteorology Interaction Airborne Field Investigations: Using lessons learned from the US west coast in the design of ACTIVATE off the east coast. *Bull. Am. Meteor. Soc.*, **100**, 1512–1528, https://doi.org/10.1175/BAMS-D-18-0100.1.

Accepted for publication in *Journal of the Atmospheric Sciences.* DOI 10.1175/JAS-D-23-0203.1.

Sorooshian, A., and Coauthors, 2023: Spatially-coordinated airborne data and complementary products for aerosol, gas, cloud, and meteorological studies: The NASA ACTIVATE dataset. *Earth Sys. Sci. Data*, https://doi.org/10.5194/essd-2023-109.

Sotiropoulou, G., S. Sullivan, J. Savre, G. Lloyd, T. Lachlan-Cope, A. Ekman, and A. Nenes, 2020: The impact of secondary ice production on Arctic stratocumulus. *Atmos. Chem. Phys.*, **20**, 1301–1316, https://doi.org/10.5194/acp-20-1301-2020.

Takahashi, T., Y. Nagao, and Y. Kushiyama, 1995: Possible high ice particle production during graupel–graupel collisions. *J. Atmos. Sci.*, **52**, 4523–4527, https://doi.org/10.1175/1520-0469.

Thornhill, K. L., B. E. Anderson, J. Barrick, D. Bagwell, R. Friesen, and D. Lenschow, 2003: Air motion intercomparison flights during Transport and Chemical Evolution in the Pacific (TRACE-P)/ACE-ASIA. *J. Geophys. Res.*, **108**, https://doi.org/10.1029/2002JD003108.

Tornow, F., A. S. Ackerman, A. M. Fridlind, G. Tselioudis, B. Cairns, D. Painemal, and G. Elsaesser, 2023: On the impact of a dry intrusion driving cloud-regime transitions in a midlatitude cold-air outbreak. *J. Atmos. Sci.*, **80**, 2881–2896, https://doi.org/10.1175/JAS-D-23-0040.1.

Tornow, F., and Coauthors, 2022: Dilution of boundary layer cloud condensation nucleus concentrations by free tropospheric entrainment during marine cold air outbreaks. *Geophys. Res. Lett.*, **49**, https://doi.org/10.1029/2022GL098444.

Vaillant de Guélis, T., A. Schwarzenböck, V. Shcherbakov, C. Gourbeyre, B. Laurent, R. Dupuy, P. Coutris, and C. Duroure, 2019: Study of the diffraction pattern of cloud particles and the respective responses of optical array probes. *Atmos. Meas. Tech.*, **12**, 2513–2529, https://doi.org/10.5194/amt-12-2513-2019.

Vömel, H., A. Sorooshian, C. Robinson, T. J. Shingler, K. L. Thornhill, and L. D. Ziemba, 2023: Dropsonde observations during the Aerosol Cloud meTeorology Interactions oVer the western ATlantic Experiment. *Scientific Data*, https://doi.org/10.1038/s41597-023-02647-5.

Welti, A., and Coauthors, 2020: Ship-based measurements of ice nuclei concentrations over the arctic, atlantic, pacific and southern oceans. *Atmos. Chem. Phys.*, **20**, 15 191–15 206.

Accepted for publication in *Journal of the Atmospheric Sciences*. DOI 10.1175/JAS-D-23-0203.1.

Wendisch, M., and Coauthors, 2019: The arctic cloud puzzle: Using acloud/pascal multiplatform observations to unravel the role of clouds and aerosol particles in arctic amplification. *Bull. Am. Meteor. Soc.*, **100 (5)**, 841 – 871, https://doi.org/10.1175/BAMS-D-18-0072.1.

Wood, R., 2005: Drizzle in stratiform boundary layer clouds. part ii: Microphysical aspects. *J. Atmos. Sci.*, **62**, 3034–3050.

Wood, R., C. S. Bretherton, D. Leon, A. D. Clarke, P. Zuidema, G. Allen, and H. Coe, 2011: An aircraft case study of the spatial transition from closed to open mesoscale cellular convection over the Southeast Pacific. *Atmos. Chem. Phys.*, **11**, 2341–2370, https://doi.org/10.5194/acp-11-2341-2011.

Young, G. S., D. A. R. Kristovich, M. R. Hjelmfelt, and R. C. Foster, 2002: Rolls, streets, waves, and more: A review of quasi-two-dimensional structures in the atmospheric boundary layer. *Bull. Am. Meteor. Soc.*, **83**, 997 – 1002, https://doi.org/https://doi.org/10.1175/1520-0477(2002)083⟨0997:RSWAMA⟩2.3.CO;2.

Zaremba, T. J., R. M. Rauber, G. M. McFarquhar, P. J. DeMott, J. J. D'Alessandro, and W. Wu, 2021: Ice in southern ocean clouds with cloud top temperatures exceeding - 5 Celsius. *J. Geophys. Res.*, **126**, https://doi.org/10.1029/2021JD034574.

Zuidema, P., and K. F. Evans, 1998: On the validity of the independent pixel approximation for boundary layer clouds observed during ASTEX. *J. Geophys. Res.*, **103**, 6059–6074.

Zuidema, P., D. Painemal, S. deSzoeke, and C. Fairall, 2009: Stratocumulus cloud top height estimates and their climatic implications. *J. Clim.*, **22**, 4652–4666, https://doi.org/10.1175/2009JCLI2708.1.

Accepted for publication in *Journal of the Atmospheric Sciences.* DOI 10.1175/JAS-D-23-0203.1.